HOKKAIDO UNIVERSITY

Title	Studies on Plasmon-induced Photoexcitation Processes of Molecules on Metal Surfaces
Author(s)	,
Citation	. ( ) 11472
Issue Date	2014-03-25
DOI	10.14943/doctoral.k11472
Doc URL	http://hdl.handle.net/2115/58193
Type	theses (doctoral)
File Information	Fumika_Nagasawa.pdf

Instructions for use

Studies on Plasmon-induced Photoexcitation Processes

of Molecules on Metal Surfaces

金属表面上における分子のプラズモン誘起光励起過程

に関する研究

Fumika Nagasawa

Graduate School of Chemical Sciences and Engineering
Hokkaido University

2014

Contents

Chapter1

General Introduction

Photoexcitation process is the basis for photochemical/physical technologies, such as photoenergy conversion, artificial photosynthesis and light emitting diode. If we find a break through to control photoexcitation processes, thechnologies could be improved drastically. The interaction between light and molecules are very restricted by the intrinsic electronic structure of material. Then it is well known about the limitation of the maximum strength of interaction at the optimal electronic structure. To solve this limitation, I applied the surface plasmon (SP) for photoexcitation of materials. SP is the collective oscillation of the free electron at metal surface. Then, the highly-confined and anisotropic electromagnetic field localized near the metal surface can be induced by the light illumination. The electromagnetic field can be affect to the materials which is located on the metal surface. The specified direction of electromagnetic field will evaluate the transition of the electronic state of target material. And a specified energy at SP state may satisfy the resonant condition with the molecular excitonic energy. It is also expected to generate and control of the coupled state between the molecular exciton and SP energy.

1.1 Surface Plasmon resonance for control of the photon field

It is suitable to use surface plasmon for confinement of the photon field near the metal surface. Highly localized electromagnetic (EM) field near the metal surface induces the enhancement phenomenon such as surface enhanced fluorescence and surface-enhanced Raman scattering. To control the energy, wavenember, and the anisotropy of the EM field, these systems

combining metals and dielectric materials for surface plasmon resonance (SPR) have been developed.

In the state of the free movement of the ion or electron (plasma), it is called plasmon that the collective oscillation of free ion or electron. In the metal, rich free electrons oscillate collectively (plasmon). The collective oscillation propagating in the bulk metal is longitudinal wave which forbidden the interaction to transverse wave of EM field. At the surface of the metal, surface plasmon propagating at the metal / dielectric interface is weeping to dielectric as evanescent field. The EM field of evanescent field has the component of transverse wave. If the surface become very confined area around a few-hundred nm such as metal nano-particle, the EM field is quantized.

For the excitation of the surface plasmon resonance, Otto configuration[1] and Kretschmann configuration[2, 3] were reported in 1968. Otto configuration was experimentally realized by using a prism on top of a metal surface with a small air gap, as depicted schematically in Figure 1.1 (a). Prism was made from the dielectric medium with high refractive index for increment of the wave-vector. The evanescent field caused by total internal reflection on the prism surface couple to the evanescent field of surface plasmon on the metal surface. The appropriate air gap distance causes the excitation of surface plasmon by light illumination. Kretschmann configuration is depicted schematically in Figure 1.1 (b) which has the interchanged configuration of metal and air. In Kretschmann configuration energy were exchanged between the evanescent wave and surface plasmon on the side of air. Otto configuration and Kretschmann configuration were reffered to collectively as attenuated total reflection (ATR).
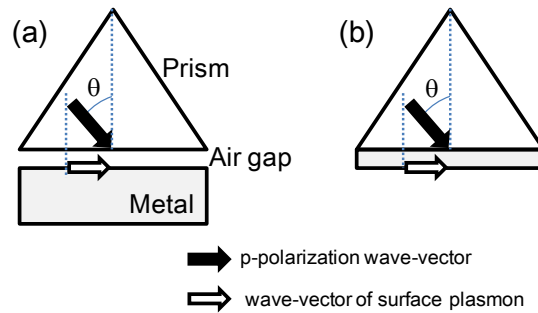
Figure 1.1 Otto configuration(a) and Kretschmann configuration(b).

More effective excitation for propagating surface plasmon without prism, diffraction grating[4, 5], sub-wavelength hole arrays[6, 7], bullseye structure[8] were adopted. The incident light wave by the diffraction can couple to the surface plasmon. These structures as a whole are called plasmonic crystal which is similar to photonic crystal. The thin film of diffraction grating whose surface plasmon couples to reverse side of metal film provide the ability to propagate coupled plasmon to far away[9]. In this mode, propagation length is long and the loss is small (so that this is called long-range plasmon[10]). This mode was first reported by Fukui et al on the thin flat film layer [11].

In a similar fashion, nano-sized metal particle can interact with light. The phenomenon is called localized surface plasmon resonance (LSPR). LSPR is induced in many structures, such as nanosphere, nano-dimer, nanorod and nanoshell[12]. Electromagnetic field of the LSPR is induced in the proximity of the metal surface, in other words, incident electromagnetic field is confined and enhanced near the metal surface. The polarization of plasmon resonance which oscillates in the same frequency to the incident light can radiate propagating wave to infinity. Appropriate proximity shows the plasmonic coupling between LSPR and LSPR, SPR and SPR, SPR and LSPR. In the condition of same resonant frequency and strong coupling between two plasmonic mode, these mode cause the hybridization which is called normal mode splitting. Interference between two modes, in phase and out phase mode, is measured. Nano-dimer structure organized from nanoparticle pair is the simplest

3

case. In phase plasmon mode is easily excited by the light and electromagnetic field is strongly

confined in the gap. Enhanced EM field shows the same direction to the excited polarization to the

parallel to the dimer long axis. Figure 1.2 show the plasmon coupling materials. If we change the

one nanoparticle of the dimer to cavity, nano-shell structure[13-17] is fabricated. More asymmetric

structure provide metamaterial[18] (Figure 1.2, b) and magnetic atoms feature[19] (Figure 1.2, c). The

electromagnetic induced transparency and fano resonance are occur when one plasmonic mode has

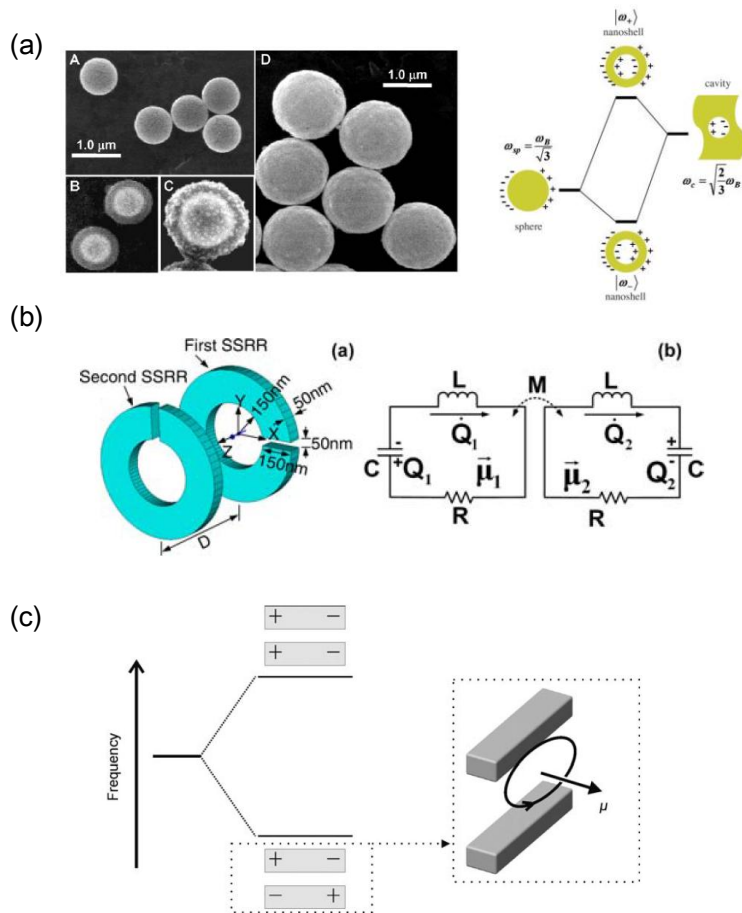the high loss and the another has the low loss.

(a)

(b)

(c)

Figure 1.2. plasmonic coupling: Nano shell[20](a), metamaterials(b)[18], magnetic atoms(c)[19].
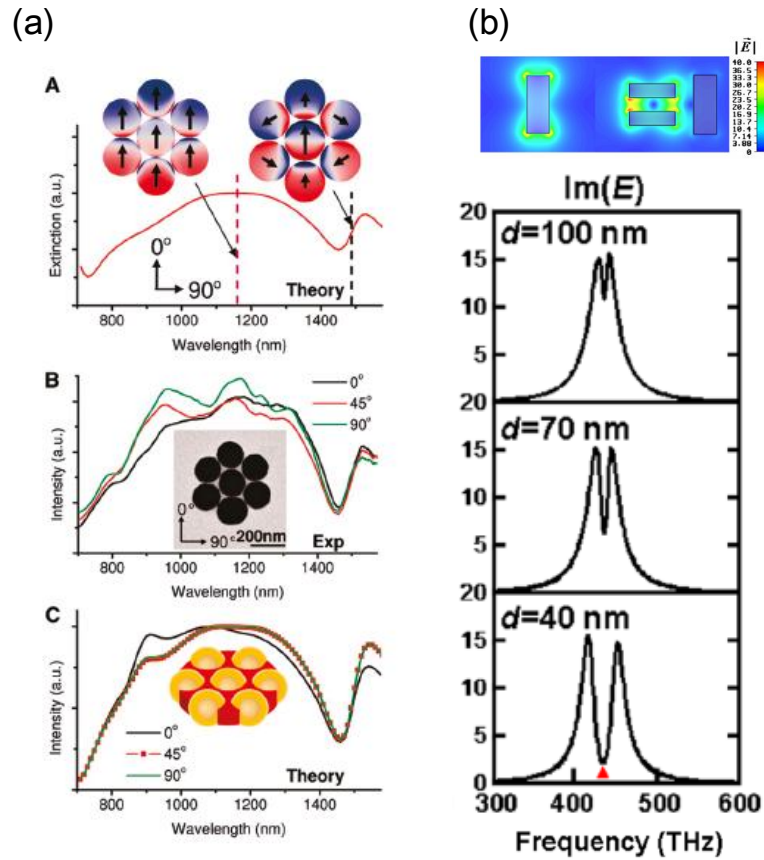
Figure 1.3. Fano resonance[21], plasmon induced transparency in metamaterial[22].

First observation of fano resonance is Wood's anomaly[23]. This structure showed the interference between incident light and reradiation from the surface plasmon. The coupling between plasmon and plasmon were measured in the heptamer of Au nanoparticles[21]. The electromagnetic induced transparency is also caused by plasmonic mode coupling[22]. Figure 1.3(b) show the EM induced transparency at the resonant frequency. Energy transfer between plasmon and plasmon is effectively induced. Fabrication technique opens the wide research avenue to control and modulate the range of photonic and optical properties.

1.2 Interaction between plasmon and molecule : Active plasmonics

The interaction between metal and molecule should be controlled to enhance the signal modulation. There is a perturbation of LSP at the gap structure as a plasmonic source. In the below, these kind of structures provides fascinating character toward intrinsic feature of interaction, which is called as *active plasmonics*.

1.2.1   To use the plasmon as confined photon field (electromagnetic enhancement)

We can use plasmonic structure as confined photon source which has enhanced electromagnetic field. These feature are known as EM effect, Purcell effect[24], plasmon resonance energy transfer (PRET)[25], plasmophore[26, 27]. These basic mechanism are used for application such as plasmon enhanced solar cell (dye sensitized solar cell[28, 29], Silicon light harvesting device[30, 31]), organic emitting light device[32]. Plasmon resonance is concern to excitation and radiation process. In the excitation process, the plasmonic resonance induces the electromagnetic effect of incident light. This effect is considered to same effect that strong light irradiate to molecules when weak light irradiates to plasmonic structure. In another process show the enhancement of radiation efficiency. As is the case of Fermi's golden rules, each molecule has the intrinsic emission rate in the nature. But if surrounding environment is modulated, the emission rate is affected. When molecules situated in the plasmonic cavity, the radiative emission rate, non-radiative emission and hole-electron coupling were changed. Radiative emission of photons is occurred in the appropriate proximity. The merits of using plasmonic structure as photon source are the enhanced excitation efficiency and quantum efficiency for suppression of non-radiative process. First pioneer observation of the plasmonic solar cell is shown in Figure 1.4 (a)[28]. This organic solar cell provided enhanced photocurrent by using the propagating surface plasmon resonance on the flat metal surface in

Kretschmann configuration. The observed enhancement is due to the increase in the photocarrier generation, which results from the enhanced light absorption under the SPP excitation. Similar enhancement mechanism is measured in the plasmon enhanced fluorescence in Figure 1.4 (b)[33]. The gap distance between tip embedded metal nanoparticle and fluorescence molecules affects the fluorescence intensity. However quenching occurred in the most proximity, maximum fluorescence intensity is measured in the appropriate gap distance. Other measurements and applications, such as plasmon enhanced Si solar cell[30, 31, 34-36], plasmonic light emitting diode[37-39] and plasmonic laser[40-43], are adopted by using electromagnetic enhancement mechanism.
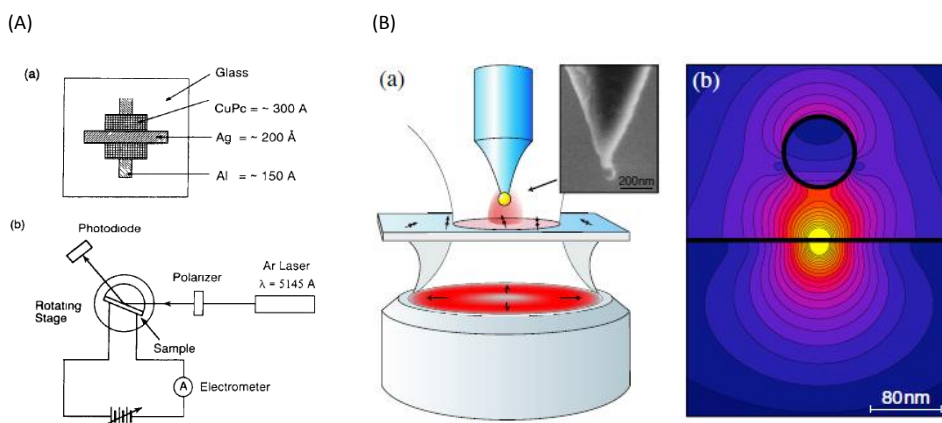

Figure 1.4. plasmonic enhanced organic solar cell(A)[28], and plasmonic enhanced fluorescence(B)[33].

1.2.2 To use the plasmon for generating electron-hole pair by plasmon decay

In contrast to electromagnetic enhancement in section 1.2.1, another important property of optical antenna is their tendency for generating energetic or "hot" electron-hole paries by plasmon decay[44-49]. Light is absorbed, forming electron-hole pair. This process of hot-electron generation has been shown to participate in photochemical reactions at noble metal nanoparticle surface[50-54]. Using hot electron is applicable for photo-energy conversion[55]. Plasmon active nanoparticles themselves perform the photocurrent generation as sensitizer[56-59]. This technique for the photo energy

7

conversion is expected to improve the conversion efficiency and extend to the absorption wavelength region to the longer wavelength.
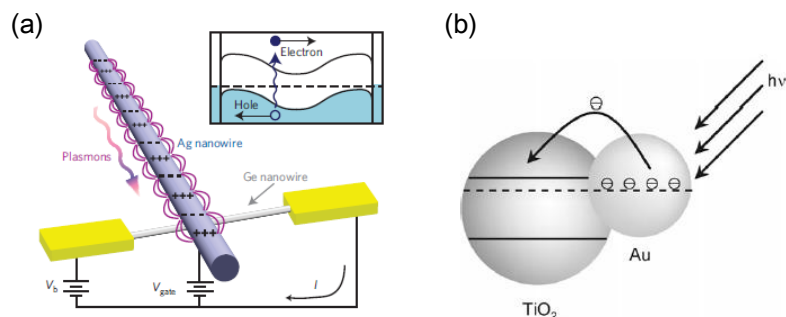

Figure 1.5. Propagating plasmon induced photo-current measurement (a)[55], photo-current measurement by using plasmonic Au nano-particles (b)[56].

1.2.3 Formation of the hybridized state

Intensive investigations of the interactions between the electronic states in organic molecules and plasmons have been undertaken. We know that organic dye molecules can have high oscillator strengths that form strong coupling regimes at room temperature[60-68]. The coupling strength can be controlled via the plasmon energy and its line widths. Recently, it has been found that hybrid states modulate the optical absorption and emission properties[60-62], the lifetimes of the excited states[63], and also the chemical reactivity[67] of the systems. Although many reports have observed strong coupling in the field of surface plasmons, application of the LSPR remains a challenging subject[69-73].
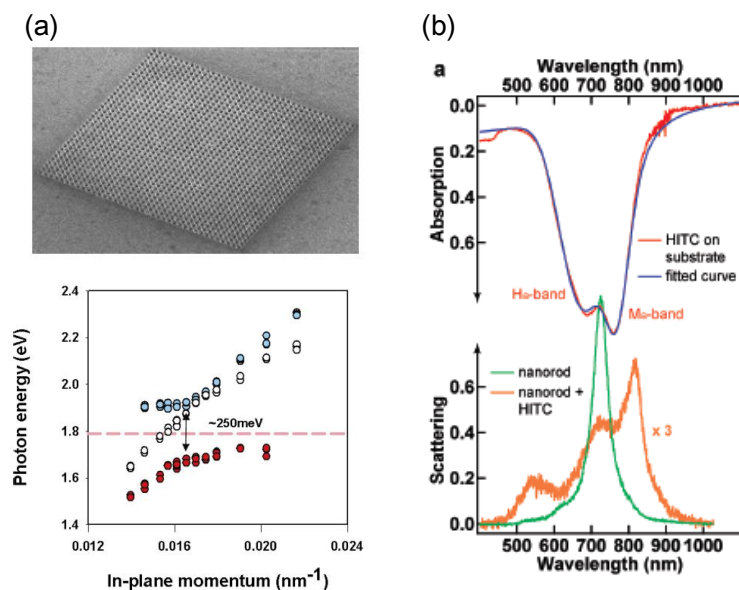
Figure 1.6. Strong coupling between organic dye molecule and propagating nano-hole surface plasmon (a)[64] and localized surface plasmon (b)[72].

1.3 Surface-enhanced Raman scattering (SERS)

Plasmon resonance is very useful technique for photoexcited and photoinduced processes. In this resonant condition, it is important to analyze the molecules which situated on the metal surface. Response of molecules at vibrational spectroscopy technique is enhanced by using surface plasmon resonance, via surface enhanced phenomena. Raman scattering is one of the useful techniques to be accurate in the identification of molecules and to perform in-situ and nondestructive. It is good design at the in-situ Raman measurement of interface between metal and molecular for using the plasmonic enhancenement field. Raman scattering is two photon processes which include the information about the excitation and the scattering. The benefit of this double resonance condition provides the strongly enhanced photon field at the edge of the metal nanostructure. It should be promising technique for extract of the information about the electronic states of the target

9

molecules at metal surface. Furthermore, it is known that Raman scattering intensity is also enhanced by the resonance of the electronic excitation at the electronic states at interface between molecules and metals. Enhanced Raman signals via various mechanisms can provide information on chemisorbed and physisorbed molecules on metal surfaces.

1.3.1 Normal Raman scattering

Polarizability of the metal nanodimer array show the intense measurement, our signal enhancement show the minimum survey at the intrinsic enhancement.

Raman polarizability of molecules is given

$$\alpha = \alpha_0 + \left(\frac{\partial \alpha}{\partial Q} \right)_0 Q \qquad (1.1)$$

$$Q = Q_0 \cos 2\pi vt \qquad (1.2)$$

$$E = E_0 \cos 2\pi vt \qquad (1.3)$$

The induced dipole moment is shown

$$\mu = \alpha E \qquad (1.4)$$

$$\mu = \alpha_0 E_0 \cos 2\pi v_i t + \frac{1}{2} \left(\frac{\partial \alpha}{\partial Q} \right)_0 Q E_0 \left[\cos 2\pi (v_i + v)t + \cos 2\pi (v_i - v)t \right] \quad (1.5)$$

The first term indicate the Rayleigh scattering, second term is correspond to Raman scattering. We can obtain the Raman scattering light, if the derived polarizability become nonzero.

$$\left(\frac{\partial \alpha}{\partial Q} \right)_0 \neq 0 \qquad (1.6)$$

This correlation is satisfy when the polarizability change with the vibration. Polarizability is derived by the polarization tensor in the space coordination.

$$\alpha = \begin{pmatrix} \alpha_{xx} & \alpha_{xy} & \alpha_{xz} \\ \alpha_{yx} & \alpha_{yy} & \alpha_{yz} \\ \alpha_{zx} & \alpha_{zy} & \alpha_{zz} \end{pmatrix} \qquad (1.7)$$

Totally symmetric mode has the diagonal element and non-totally symmetric mode has the non-diagonal element. The electromagnetic unit vector is represented by tensor, which we can denote the polarization configuration.

$$\mathbf{e}_i = \begin{pmatrix} x \\ y \\ z \end{pmatrix}, \quad \mathbf{e}_s = \begin{pmatrix} x \\ y \\ z \end{pmatrix} \qquad (1.8)$$

We can deduce the Raman intensity($I_s R^2$) as shown below

$$I_s R^2 = \frac{\omega_s^4}{c^4} (\mathbf{e}_s \alpha \mathbf{e}_i)^2 I_i \qquad (1.9)$$

I_i is intensity of the incident planar electromagnetic wave, ω_s is angular frequency of scattering photon. The both of the incident polarization and scattering polarization is related to the intensity of the Raman scattering.

If the polarized Raman measurement were performed, the intensity ratio of the Raman spectrum is changed in each orientation to the intrinsic polarization configuration. For example, in the backscattering configuration which has the 0° between incident and scattering propagating direction, when we use the parallel incident and scattering polarization to the x-direction, the intensity ratio at the each polarization in each polarization angle, the tensor element of α_{xx} engages the Raman scattering intensity. The system of the single crystal of molecules which is fixed at the specific orientation in the space enables us to measure the tensor elements. However the liquid or the solution in which molecules oriented randomly show the random tensor elements. If we consider about the depolarization ratio, we can analyze whether totally symmetric mode or non-totally symmetric mode. Depolarization ratio ρ is defined by the ratio of the Raman intensity

11

of perpendicular polarization to parallel polarization. Totally symmetric mode show $0 \leq \rho < 0.75$ and non-totally symmetric mode show $\rho = 0.75$.

1.3.2 Electromagnetic effect of SERS

If we use the metal nanoparticle, Raman signal is strongly enhanced by induced localized surface plasmon resonance. Surface-enhanced Raman scattering intensity is determined as below.

$$I_s R^2 = \frac{8\pi(\omega \pm \omega_{IF})^4}{9c^4} I_L \sum_{\sigma,\rho} |\alpha_{\sigma\rho}|^2 \quad (1.10)$$

I_L is the intensity of the incident planar electromagnetic wave, ω_{IF} is angular frequency of scattering photon, $\mathbf{e}$ is electronic vector. The intensity of the Raman scattering is determined by the both of the incident and scattering electromagnetic field like normal Raman process. Intense Raman enhancement is originated from the twofold electromagnetic enhancement mechanism, which arise from coupling of plasma resonance with both incident and Raman scattering light[74-77]. First, the light shines to the metal nanoparticles, LSPR absorption will occur. Then, localized surface Plasmon resonance is excited, and Raman scattering radiation will occur in the region of the intense Raman enhancement when incident photon will resonant with the scattering photon energy. Excited plasmon resonance radiates the scattering photon once again. The twofold EM enhancement theory is estimated about 10^{14} enhancement of Raman scattering intensity of the incident light intensity. The equation of the enhancement of the Raman intensity were shown below

$$I \propto \frac{8\pi(\omega \pm \omega_{IF})^4}{9c^4} I_L L^2(\omega) L^2(\omega_{IF}) \sum_{\rho,\sigma} |\alpha_{\rho\sigma}|^2 \quad (\alpha_{\sigma,\rho} = x, y, z) \quad (1.11)$$

L is electromagnetic enhancement factor. The electromagenetic enhancement factor as a function of the light energy shows the intense field at the incident (ω) and/or scattering (ω_{IF}) enegy. In this

theory, L is also concern with the Raman enhancement at each polarization direction. The polarization direction is also important to decide both of Raman enhancement factor and active mode of vibration.

1.3.3 Electronic (and vibronic) resonance Raman scattering

When the incident light energy is close to the particular molecular absorption band, the intensity of Raman scattering shows the enhancement in some orders as incident photonfield. In the quantum mechanical theory, Polarizability tensor is derived from the Kramers-Heisenberg-Dirac (KHD) dispersion equation.

$$\alpha_{\rho\sigma} = \sum_{e \neq m,n} \left\{ \frac{\langle I | \mu_\sigma | K \rangle \langle K | \mu_\rho | F \rangle}{E_K - E_I - \hbar\omega - i\Gamma} + \frac{\langle I | \mu_\rho | K \rangle \langle K | \mu_\sigma | F \rangle}{E_K - E_F + \hbar\omega + i\Gamma} \right\} \qquad (1.\ 12)$$

$|I\rangle$ is ground state, $|F\rangle$ is final state, $|K\rangle$ is intermediate state. In the normal (this term means non-resonant condition) Raman scattering, $E_K - E_I \rangle\rangle \hbar\omega$ is satisfy and the term of the energy denominator $E_K - E_I - \hbar\omega$ become almost the same of the all intermediate states. In the resonant Raman scattering, $E_K - E_I \approx \hbar\omega$ is consisted and specific vibrational mode which has small energy denominator $E_K - E_I - \hbar\omega$ show the Raman enhancement in some order.

In the non-resonant condition, it is sufficient to use the Born-Oppenheimer approximation. Born-Oppenheimer approximation neglects coupling between electronic and nuclear motions. However, in the resonant condition, the electronic transition moment has a slight dependence on the normal coordinates of vibration Q and coupling Hamiltonian may be expressed by an expansion in the nuclear displacement (Herz-Teller expansion). We will obtain the polarizability tensor in the form,

$$\alpha_{\rho\sigma} = A + B + C + D \qquad (1.13)$$

where

$$A = \sum_{K \neq I} \sum_{k} \frac{M_{KI}^{\sigma}(Q_0) M_{KI}^{\rho}(Q_0)}{\hbar(\omega_{KI} - \omega) - i\Gamma} \langle i|k \rangle \langle k|f \rangle \qquad (1.14)$$

$$B = \sum_{K \neq I} \sum_{k} \sum_{M \neq K} \left[\frac{M_{IK}^{\sigma} h_{KM} M_{MI}^{\rho}}{\hbar(\omega_{KI} - \omega) - i\Gamma} \right] \frac{\langle i|k \rangle \langle k|Q|f \rangle}{\hbar \omega_{MK}}$$

$$+ \sum_{K \neq I} \sum_{k} \sum_{M \neq K} \left[\frac{M_{IM}^{\sigma} h_{MK} M_{KI}^{\rho}}{\hbar(\omega_{KI} - \omega) - i\Gamma} \right] \frac{\langle i|Q|k \rangle \langle k|f \rangle}{\hbar \omega_{MK}} \qquad (1.15)$$

$$C = \sum_{K \neq I} \sum_{k} \sum_{M \neq I} \left[\frac{h_{IM} M_{MK}^{\sigma} M_{KI}^{\rho}}{\hbar(\omega_{KI} - \omega) - i\Gamma} \right] \frac{\langle i|k \rangle \langle k|Q|f \rangle}{\hbar \omega_{IM}}$$

$$+ \sum_{K \neq I} \sum_{k} \sum_{M \neq I} \left[\frac{M_{IK}^{\sigma} M_{KM}^{\rho} h_{MI}}{\hbar(\omega_{KI} - \omega) - i\Gamma} \right] \frac{\langle i|Q|k \rangle \langle k|f \rangle}{\hbar \omega_{IM}} \qquad (1.16)$$

$$D = \sum_{K \neq M} \sum_{k} \sum_{I \neq M} \left[\frac{M_{IK}^{\sigma} h_{KM} h_{MK} M_{KI}^{\rho}}{\hbar(\omega_{IM} - \omega) - i\Gamma} \right] \frac{\langle i|Q|k \rangle \langle k|Q|f \rangle}{\hbar^2 \omega_{MK}} \qquad (1.17)$$

In figure 1. each transition electronic dipole for Raman processes is described. A-term is described by the Franck-Condon factor $\langle i|k \rangle \langle k|f \rangle$. In B-term, it will be the degree of the vibronic coupling between one electronic state and another one. Each vibronic coupling is described the dotted line in Figure 1.7. As the energy separation of the ground electronic state and the excited electronic state is normally large the C and D term is likely to be negligible and we shall not consider in resonant Raman condition.
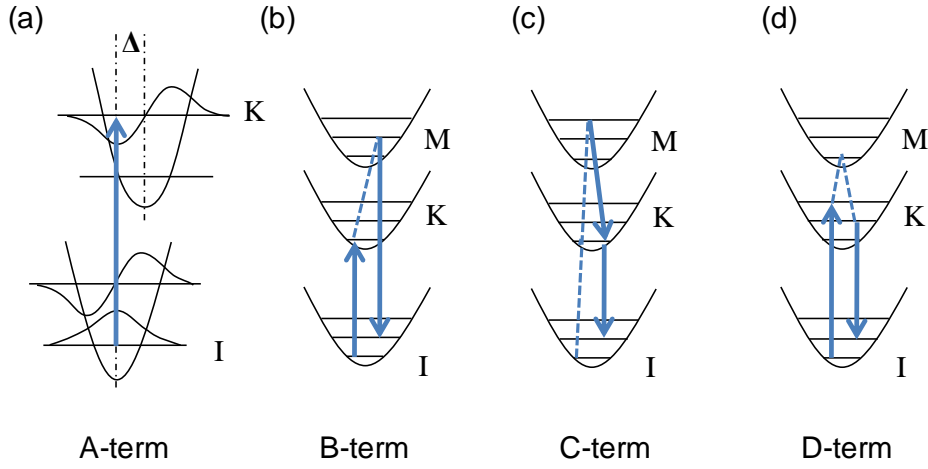
(a)   (b)   (c)   (d)

A-term   B-term   C-term   D-term

Figure 1.7 The transition electronic dipole products which occur in the numerator of selectrd term of A, B, C, D in eqs. (1. 14) to (1. 17).

1.3.4 Chemical effect of SERS

In the SERS system, there is some additional enhancement in the non-totally symmetric mode of vibration. This appearance of additional mode is not explained by the mechanism of EM effect. This origin is known to be chemical effect via charge transfer from metal (or molecule) to molecule (or metal). When the resonant condition is satisfied between charge transfer energy and excitation energy, polarization is shown

$$\alpha_{\rho\sigma} = A_f + A_k + B + C \quad (1.\ 18)$$

where

$$A_f = \frac{2}{\hbar} \sum_M M_{MI}^{\sigma} M_{MI}^{\rho} \langle i|k\rangle\langle k|f\rangle \frac{\omega_{MI} + \omega_f}{\left(\omega_{MI} + \omega_f\right)^2 - \omega^2} \qquad (1.\ 19)$$

$$A_k = \frac{2}{\hbar} \sum_M M_{KM}^{\sigma} M_{KM}^{\rho} \langle i|k\rangle\langle k|f\rangle \frac{\omega_{KM} + \omega_k}{\left(\omega_{KM} + \omega_k\right)^2 - \omega^2} \qquad (1.\ 20)$$

$$B = -\frac{2}{\hbar} \sum_{K \neq I} \sum_{M < K} M_{KI}^{\sigma} M_{MI}^{\rho} h_{KM} \langle i|Q|f \rangle \frac{\left(\omega_{KI} \omega_{MI} + \omega^2 \right)}{\left(\omega_{KI}^2 - \omega \right) \left(\omega_{MI}^2 - \omega \right)} \tag{1.21}$$

$$C = -\frac{2}{\hbar} \sum_{K \neq I} \sum_{M > I} M_{MK}^{\sigma} M_{KI}^{\rho} h_{IM} \langle i|Q|f \rangle \frac{\left(\omega_{KI} \omega_{KM} + \omega^2 \right)}{\left(\omega_{KI}^2 - \omega^2 \right) \left(\omega_{KM}^2 - \omega^2 \right)} \tag{1.22}$$

These resonant condition are schematically shown in Figure 1.8. The transition electronic dipole is shown in arrowed line. When the excitation energy is resonant to the each transition energy, term in the polarizability tensor is enhanced and Raman activity enlarges.
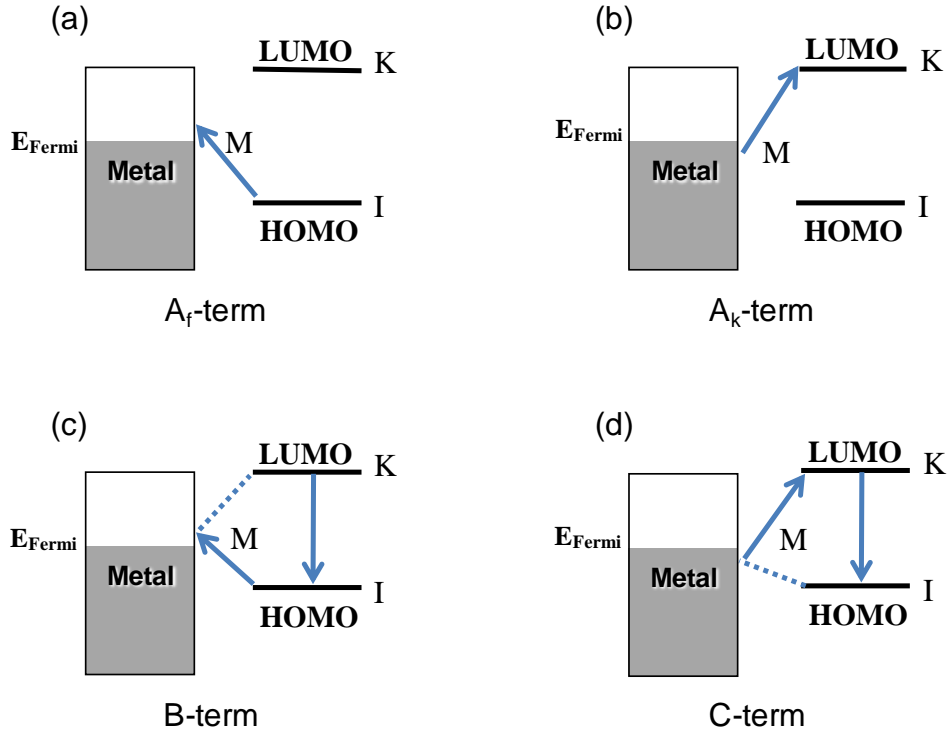

Figure 1.8. The transition electronic dipole products which occur in the numerator for term of A_f, A_k, B, C in eqs. (1. 18) to (1. 22).

1.4 The aim of this study

If the molecules situated on the metal nanoparticle surface shined the light, many photoexcitation processes will occur. And plasmonic enhanced phenomena can obtain molecular vibrational information easily by using Raman scattering.

First, I fabricated the highly ordered nanostructure and evaluated the polarization of the SERS scattering photons (Chapter 2). Then conductance measurement at the junction of the metal-molecule-metal system proved the SERS depolarization and charge transfer behavior in the interface between metal and molecule (Chapter 3). In the electrochemical environment, photoexcitation processes were evaluated by using single walled carbon nanotube in the metal nano-gap (Chapter 4). For more active modulation of photoexcitation process in the hybrid system of molecule and metal, strong coupling regime between molecular excitons and plasmon resonance of metal nano-particle was achieved (Chapter 5). Resonant condition in the hybridized state was controlled by using electrochemical potential tuning (Chapter 6).

The result of this study will offer a novel molecular photoexcitation process which is localized near the metal surface. And the new hybrid state of LSP supposed to modulate the intrinsic energy which excites the molecules or plasmonic metal nanoparticles. These techniques gave the insight to fabricate the new photoexcitation energy state at the interface.

1.5 References

1. Otto, A. *Z. Physiks.* **1968,** 216, 398.

2. Kretschman, E.; Raether, H. *Z. Naturfors* **1968,** 23a, 2135.

3. Kretschmann, E. *Z. Physik.* **1971,** 241, 313.

4. Ritchie, R. H.; Arakawa, E. T.; Cowan, J. J.; Hamm, R. N. *Phys. Rev. Lett.* **1968,** 21, 1530-1533.

5. Pockrand, I. *Opt. Commun.* **1975,** 13, 311-313.

6. Ebbesen, T. W.; Lezec, H. J.; Ghaemi, H. F.; Thio, T.; Wolff, P. A. *Nature* **1998,** 391, 667-669.

7. Ghaemi, H. F.; Thio, T.; Grupp, D. E.; Ebbesen, T. W.; Lezec, H. J. *Phys. Rev. B* **1998,** 58, 6779-6782.

8. Ishi, T.; Fujikata, J.; Ohashi, K. *Jpn. J. Appl. Phys., Part 2* **2005,** 44, L170-L172.

9. Hooper, I. R.; Sambles, J. R. *Phys. Rev. B* **2004,** 70, 045421.

10. Sarid, D. *Phys. Rev. Lett.* **1981,** 47, 1927-1930.

11. Fukui, M.; So, V. C. Y.; Normandin, R. *Phys. Stat. Solidi (b)* **1979,** 91, K61-K64.

12. Halas, N. J.; Lal, S.; Chang, W.-S.; Link, S.; Nordlander, P. *Chem. Rev.* **2011,** 111, 3913-3961.

13. Lindquist, N. C.; Jose, J.; Cherukulappurath, S.; Chen, X.; Johnson, T. W.; Oh, S.-H. *Laser & Photon. Rev.* **2013,** 7, 453-477.

14. Bartczak, D.; Muskens, O. L.; Sanchez-Elsner, T.; Kanaras, A. G.; Millar, T. M. *ACS Nano* **2013,** 7, 5628-5636.

15. Terekhin, V. V.; Zaitseva, A. V.; Dement'eva, O. V.; Rudoy, V. M. *Colloid J.* **2013,** 75, 437-443.

16. Borys, N. J.; Shafran, E.; Lupton, J. M. *Sci. Rep.* **2013,** 3.

17. Le Thi Ngoc, L.; Jin, M.; Wiedemair, J.; van den Berg, A.; Carlen, E. T. *ACS Nano* **2013,** 7, 5223-5234.

18. Liu, H.; Liu, Y. M.; Li, T.; Wang, S. M.; Zhu, S. N.; Zhang, X. *Phys. Stat. Solidi (b)* **2009,** 246, 1397-1406.

19. Liu, N.; Giessen, H. *Angew. Chem. Int. Ed.* **2010,** 49, 9838-9852.

20. Xue, C.; Xue, Y.; Dai, L.; Urbas, A.; Li, Q. *Adv. Opt. Mat.* **2013,** 1, 581-587.

21. Fan, J. A.; Wu, C.; Bao, K.; Bao, J.; Bardhan, R.; Halas, N. J.; Manoharan, V. N.; Nordlander, P.; Shvets, G.; Capasso, F. *Science* **2010,** 328, 1135-1138.

22. Zhang, S.; Genov, D. A.; Wang, Y.; Liu, M.; Zhang, X. *Phys. Rev. Lett.* **2008,** 101, 047401.

23. Wood, R. W. *Phil. Mag.* **1902,** 4, 396.

24. Smith, S. J.; Purcell, E. M. *Phys. Rev.* **1953,** 92, 1069-1069.

25. Liu, G. L.; Long, Y.-T.; Choi, Y.; Kang, T.; Lee, L. P. *Nat. Meth.* **2007,** 4, 1015-1017.

26.   Lakowicz, J. R.; Ray, K.; Chowdhury, M.; Szmacinski, H.; Fu, Y.; Zhang, J.; Nowaczyk, K. *Analyst* **2008,** 133, 1308-1346.

27.   Ming, T.; Zhao, L.; Chen, H.; Woo, K. C.; Wang, J.; Lin, H.-Q. *Nano Lett.* **2011,** 11, 2296-2303.

28.   Hayashi, S.; Kozaru, K.; Yamamoto, K. *Solid State Commun.* **1991,** 79, 763-767.

29.   Shinji, H.; Takayuki, O. *J. Phys. D: Appl. Phys.* **2012,** 45, 433001.

30.   Stuart, H. R.; Hall, D. G. *Appl. Phys. Lett.* **1996,** 69, 2327-2329.

31.   Stuart, H. R.; Hall, D. G. *Appl. Phys. Lett.* **1998,** 73, 3815-3817.

32.   Neal, T.; Okamoto, K.; Scherer, A. *Opt. Express* **2005,** 13, 5522-5527.

33.   Anger, P.; Bharadwaj, P.; Novotny, L. *Phys. Rev. Lett.* **2006,** 96, 113002.

34.   Catchpole, K. R.; Pillai, S. *J. Lumin.* **2006,** 121, 315-318.

35.   Pillai, S.; Catchpole, K. R.; Trupke, T.; Green, M. A. *J. Appl. Phys.* **2007,** 101, 093105-093105-8.

36.   Derkacs, D.; Lim, S. H.; Matheu, P.; Mar, W.; Yu, E. T. *Appl. Phys. Lett.* **2006,** 89, 093103.

37.   Köck, A.; Beinstingl, W.; Berthold, K.; Gornik, E. *Appl. Phys. Lett.* **1988,** 52, 1164-1166.

38.   Köck, A.; Gornik, E.; Hauser, M.; Beinstingl, W. *Appl. Phys. Lett.* **1990,** 57, 2327-2329.

39.   Hecker, N. E.; Höpfel, R. A.; Sawaki, N.; Maier, T.; Strasser, G. *Appl. Phys. Lett.* **1999,** 75, 1577-1579.

40.   Plotz, G. A.; Simon, H. J.; Tucciarone, J. M. *Journal of the Opt. Soc. Am.* **1979,** 69, 419-422.

41.   Seidel, J.; Grafström, S.; Eng, L. *Phys. Rev. Lett.* **2005,** 94, 177401.

42.   Noginov, M. A.; Podolskiy, V. A.; Zhu, G.; Mayy, M.; Bahoura, M.; Adegoke, J. A.; Ritzo, B. A.; Reynolds, K. *Opt. Express* **2008,** 16, 1385-1392.

43.   Noginov, M. A.; Zhu, G.; Mayy, M.; Ritzo, B. A.; Noginova, N.; Podolskiy, V. A. *Phys. Rev. Lett.* **2008,** 101, 226806.

44.   Hofmann, J.; Steinmann, W. *Phys. Stat. Solidi (b)* **1968,** 30, K53-K56.

45.   Inagaki, T.; Kagami, K.; Arakawa, E. T. *Phys. Rev. B* **1981,** 24, 3644-3646.

46.   Inagaki, T.; Kagami, K.; Arakawa, E. T. *Appl. Opt.* **1982,** 21, 949-954.

47.   Lehmann, J.; Merschdorf, M.; Pfeiffer, W.; Thon, A.; Voll, S.; Gerber, G. *Phys. Rev. Lett.* **2000,** 85, 2921-2924.

48.   Shalaev, V. M.; Douketis, C.; Stuckless, J. T.; Moskovits, M. *Phys. Rev. B* **1996,** 53, 11388-11402.

49.   Endriz, J. G.; Spicer, W. E. *Phys. Rev. Lett.* **1970,** 24, 64-68.

50.   Redmond, P. L.; Brus, L. E. *J. Phys. Chem. C* **2007,** 111, 14849-14854.

51.   Jin, R.; Cao, Y.; Mirkin, C. A.; Kelly, K. L.; Schatz, G. C.; Zheng, J. G. *Science* **2001,** 294, 1901-1903.

52.   Jin, R.; Cao, Y. C.; Hao, E.; Metraux, G. S.; Schatz, G. C.; Mirkin, C. A. *Nature* **2003,** 425, 487-490.

53.   Brus, L. *Acc. Chem. Res.* **2008,** 41, 1742-1749.

54.   Wu, X.; Thrall, E. S.; Liu, H.; Steigerwald, M.; Brus, L. *J. Phys. Chem. C* **2010,** 114, 12896-12899.

55.   Falk, A. L.; Koppens, F. H. L.; Yu, C. L.; Kang, K.; de Leon Snapp, N.; Akimov, A. V.; Jo, M.-H.; Lukin, M. D.; Park, H. *Nature Phys.* **2009,** 5, 475-479.

56.   Tian, Y.; Tatsuma, T. *Chem. Commun.* **2004**, 1810-1811.

57.   Tian, Y.; Tatsuma, T. *J. Am. Chem. Soc.* **2005,** 127, 7632-7637.

58.   Nishijima, Y.; Ueno, K.; Yokota, Y.; Murakoshi, K.; Misawa, H. *J. Phys. Chem. Lett.* **2010,** 1, 2031-2036.

59.   Nishijima, Y.; Ueno, K.; Kotake, Y.; Murakoshi, K.; Inoue, H.; Misawa, H. *J. Phys. Chem. Lett.* **2012,** 3, 1248-1252.

60.   Pockrand, I.; Brillante, A.; Mobius, D. *J. Chem. Phys.* **1982,** 77, 6289-6295.

61.   Lidzey, D. G.; Bradley, D. D. C.; Skolnick, M. S.; Virgili, T.; Walker, S.; Whittaker, D. M. *Nature* **1998,** 395, 53-55.

62.   Lidzey, D. G. *Science* **2000,** 288, 1620-1623.

63.   Bellessa, J.; Bonnand, C.; Plenet, J.; Mugnier, J. *Phys. Rev. Lett.* **2004,** 93, 036404.

64.   Dintinger, J.; Klein, S.; Bustos, F.; Barnes, W.; Ebbesen, T. *Phys. Rev. B* **2005,** 71, 035424.

65.   Sugawara, Y.; Kelf, T. A.; Baumberg, J. J.; Abdelsalam, M. E.; Bartlett, P. N. *Phys. Rev. Lett.* **2006,** 97, 266808.

66.   Hakala, T.; Toppari, J.; Kuzyk, A.; Pettersson, M.; Tikkanen, H.; Kunttu, H.; Törmä, P. *Phys. Rev. Lett.* **2009,** 103, 053602.

67.   Hutchison, J. A.; Schwartz, T.; Genet, C.; Devaux, E.; Ebbesen, T. W. *Angew. Chem. Int. Ed.* **2012,** 51, 1592-1596.

68.   Hutchison, J. A.; Liscio, A.; Schwartz, T.; Canaguier-Durand, A.; Genet, C.; Palermo, V.; Samori, P.; Ebbesen, T. W. *Adv. Mater.* **2013,** 25, 2481-2485.

69.   Wiederrecht, G. P.; Wurtz, G. A.; Hranisavljevic, J. *Nano Lett.* **2004,** 4, 2121-2125.

70.   Wurtz, G. A.; Evans, P. R.; Hendren, W.; Atkinson, R.; Dickson, W.; Pollard, R. J.; Zayats, A. V.; Harrison, W.; Bower, C. *Nano Lett.* **2007,** 7, 1297-1303.

71.   Fofang, N. T.; Park, T. H.; Neumann, O.; Mirin, N. A.; Nordlander, P.; Halas, N. J. *Nano Lett.* **2008,** 8, 3481-3487.

72.   Ni, W.; Ambjornsson, T.; Apell, S. P.; Chen, H.; Wang, J. *Nano Lett.* **2010,** 10, 77-84.

73.   Schlather, A. E.; Large, N.; Urban, A. S.; Nordlander, P.; Halas, N. J. *Nano Lett.* **2013,** 13, 3281-3286.

74.   Inoue, M.; Ohtaka, K. *J. Phys. Soc. Jpn.* **1983,** 52, 3853-64.

75.   Pettinger, B. *J. Chem. Phys.* **1986,** 85, 7442-7451.

76.   Xu, H.; Bjerneld, E. J.; Käll, M.; Börjesson, L. *Phys. Rev. Lett.* **1999,** 83, 4357-4360.

77.   Xu, H.; Wang, X.-H.; Persson, M. P.; Xu, H. Q.; Käll, M.; Johansson, P. *Phys. Rev. Lett.* **2004,** 93, 243002.

Chapter 2

Depolarization Behavior of

Surface-Enhanced Raman Scattering Photons

at the Metal Nano-Dimer Structure

2.1 Introduction

Interface between metal and molecule provide the highly attractive field which interact with each other, such as charge transfer. However it is hardly known about materials localized at interface. Polarized Raman measurement represents the intense research field on the metal surface. Polarized surface-enhanced Raman scattering (SERS) signal has highly polarized character because of the anisotropic electromagnetic feature on the metal surface. And these signals supposed to have high sensitivity about the electronic state at interface. Polarized SERS measurements give information on both the incident and Raman scattering polarizations. Several interesting polarized SERS studies have been carried out[1-13]. If one assumes a symmetrical single nano-dimer structure in which only the localized electromagnetic field at the gap contributes to the enhancement, SERS depolarization is not observed because the polarizations for excitation and scattering are the same. Linearly polarized scattered light was observed in a metal nano-dimer system. Haran et al. reported that an asymmetric metal nanoparticle trimer generates elliptically polarized scattered light, showing that the polarization of light scattered from molecules can be manipulated on the nanometre scale[7]. A well-accepted model of the twofold EM enhancement theory for excitation and scattering for the SERS process cannot explain the present observations, because the theory predicts that the

polarization of the scattering photons is controlled in the same manner as that of the localized field[3, 14]. On the other hand, depolarization behavior has been also reported. Polarization rotation induced by plasmon resonance of the SERS signal with respect to the incident polarization was shown in arrays of uniform Au nanostructures[11]. By using an elliptic nanostructure which exhibits two LSP resonances each associated with one of the two principle axis, scattered light is resonant with another axis to one axis of the excitation process. In the present study, polarization dependence on SERS from a well-ordered Ag dimer array[15] was measured in an aqueous solution containing the target molecule, 4,4'-bipyridine. In this chapter, polarization dependence of the scattering photons was discussed with respect to the optical properties of the metal nanostructure and adsorption structure of the target molecule.

2.2 Experimental

The Ag dimer arrays were prepared by an angle-resolved nanosphere lithography technique (AR-NSL) using repeated vapor depositions onto the polystyrene (PS) particle (Polysciences Inc.; diameters = 350 nm) monolayer prepared on a glass substrate[16]. Aqueous PS particle suspension was concentrated to 10 wt.%, and then diluted by ethanol (50 %). As well as previously documented drop-coating method, I adapted the other method using PS monolayers prepared on liquid-gas interfaces to improve the quality of the array. The PS solutions (20 μL) were dropped on convex surface of a watch glass immersed in Milli-Q water. Thin water layer on the glass surface leads to uniform spreading of PS beads on the air-water interface. After the spreading of PS beads to water surface, the layer was packed tight in the course of nature. The change in the surface tension of the water around the PS layer results in the formation of well-ordered monolayers with low density of defects, dislocations, and vacancies on the liquid-water interface. The prepared

monolayer with high quality was then lifted off from the water surface using cleaned glass substrate. The metal was deposited onto the PS monolayer prepared on the glass substrate. After the first metal deposition, the second metal was deposited with different angles. Then, the PS mask was removed by sonication in Milli-Q water for 10-30 s. Extinction spectrum of the metal dimer array in the visible-near infrared region were recorded utilizing a multi-channel spectrometer (MCPD-2000, Ohtsuka Electronics). The structure of the dimer on the glass substrate was inspected by an atomic force microscope (AFM, Nanoscope-IIIa, Digital Instruments) in air.

A home-made polarized Raman microprobe spectrometer was specially modified for NIR laser light (λ_{ex} = 785 nm). Raman measurements were carried out at the backscattering configuration collecting the scattering photons with the parallel and the perpendicular polarization directions simultaneously (Figure 2.1 (a)). The expanded NIR beam is focused onto the sample using a water-immersion objective lens with 100x magnification and a numerical aperture of 1.0. The estimated spot size of irradiation ca. 1 μm, with tunable output intensity was in the range between 10 μW and 20 mW. All of Raman measurements were carried out in-situ by immersion of the SERS active substrates into aqueous solutions containing target molecule (4,4'-bipyridine; reagent grade, Wako Co. Ltd.) with controlled concentration (1 μM – 1 mM). The measurement on a single crystal was carried out in air by controlling the excitation polarization direction to the crystal axis determined by XRD.

The stability of the metal structure was checked by the polarized Rayleigh scattering light measurement. Completely the same polarized properties were obtartained before and after the light irradiation, indicating that the metal dimer structure is stable regardless of the light irradiation.

Density functional theory (DFT) calculations were carried out by the use of the Gaussian 03, revision E.01, at the B3LYP level of DFT with 6-31G** basis sets. Calculation were carried out without the contribution of the resonance of 4,4'-bipyridine molecule. Raman intensity was

estimated using

$$I \propto \nu_s^4 \left(e_s \alpha e_i \right)^2 \quad (2.1)$$

where ν_s is the wavenumber of the Raman scattering and e_s, e_i are the unit vector along the scattering and incident electric field and α is the polarization tensor.
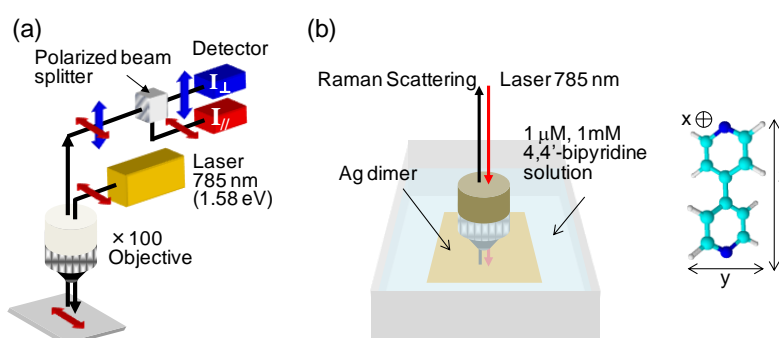

Figure 2.1 Raman measurement configuration (a), in-situ Raman cell and 4,4'-bipyridine molecular structure (b).

2.3 Results and Discussion

For Raman band assignments, conventional polarized Raman measurements were carried out using a 15 mM aqueous solution of 4,4'-bipyridine and tetrachloromethane solution (I_{ex} = 20 mW, t_{ex} = 100 s). The Raman spectrum of an aqueous solution for the parallel scattering configuration showed intense peaks at 1010 and 1298 cm^{-1} and weak peaks at 764, 873 and 1229 cm^{-1} (Fig. 2.2(a)). For the perpendicular configuration, scattering was not observed clearly (Fig. 2.2(b)). This indicates that the peaks assigned to totally symmetric a modes of 4,4'-bipyridine molecules [15, 17,18,19] have a zero depolarization ratio for an aqueous solution. Polarized Raman spectra of tetrachloromethane solution are shown in Fig. 2.2 (c) and (d). The Raman spectrum of a

ttetrachloromethane solution for the parallel scattering configuration showed the intense peaks at 218 (E), 314 (T_2), 460 cm^{-1} (A). Parallel scattering polarization which has a 3/4 depolarization ratio for nontotally symmetric modes [218 cm^{-1} (E), 314 cm^{-1}(T_2)] with linearly polarized incident light were measured.

For investigate the Raman polarized tensor I fabricated the 4,4'-bipyridine single crystal (Figure 2.3 (a)). XRD analyze show the $P2_1$ symmetry in Figure 2.3 (b) which is the similar symmetry as reported before [20]. I measured the each polarization configuration to the single crystal axis of 4,4'-bipyridine and compared to the DFT calculation. Figure 2.3 (c) shows the polarized Raman spectra of each polarization configuration (I_{ex}=20 mW, t_{ex}=10 s). For parallel polarization configuration on *a*-excitation (excitation polarization is parallel to the *a*-axis of single crystal) and *a*-scattering (scattering polarization is parallel to the *a*-axis) direction, relatively strong peak at at 762, 1000 and 1301 cm^{-1} and weak peaks at 880, 1075 and 1230 cm^{-1} were observed. For the other parallel configuration on (*b*, *b*), (*c*, *c*) it were observed same peaks and intensity ratio of peaks were changed. (*b*, *b*) configuration 1240 cm^{-1} had maximum peak intensity. On the other hand, (*c*, *c*) configuration 1000 and 1300 cm^{-1} had maximum peak intensity. For the perpendicular polarization
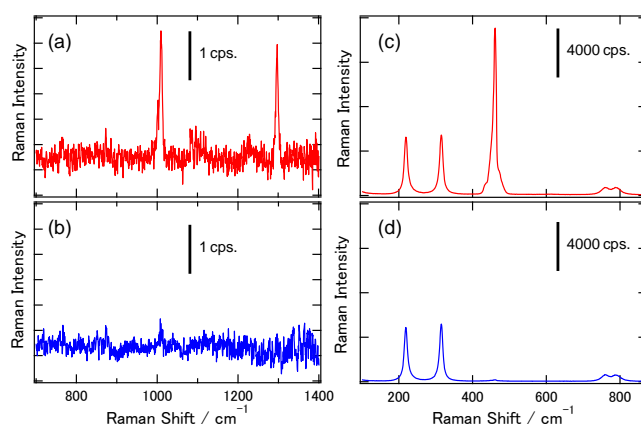

Figure 2.2 Polarized Raman spectrum in 4,4'-bipyridine solution (a,b) and tetrachloromethane solution (c,d): parallel configuration (a,c) and perpendicular polarization(b,d).

configuration on (*a*, *b*) additional peaks at 862, 1042, 1215 and 1325 cm^{-1} were observed. Polarization dependence of intensity ratio for the parallel polarization and additional peaks appearance for the perpendicular polarization were well reflected in calculated polarized Raman spectra (Figure 2.3 (d)). Perpendicular configurations are assigned to totally symmetric a modes and non-totally symmetric b1 modes of 4,4'-bipyridine molecules, respectively[15, 17-19].

Polarization dependence on SERS was measured using the substrate with an Ag dimer array (Figure 2.4 (a)). The thickness and distance of the dimer structure were optimized to provide an extinction peak around 780 nm at the parallel polarization along the long dimer axis (Figure 2.4 (b)) for the excitation of the Raman measurement (I_{ex} = 785 nm). The dimer structure consists of the different size Ag triangle. The size is 50 nm, 100 nm at each side of triangle, and the height is 25 nm,
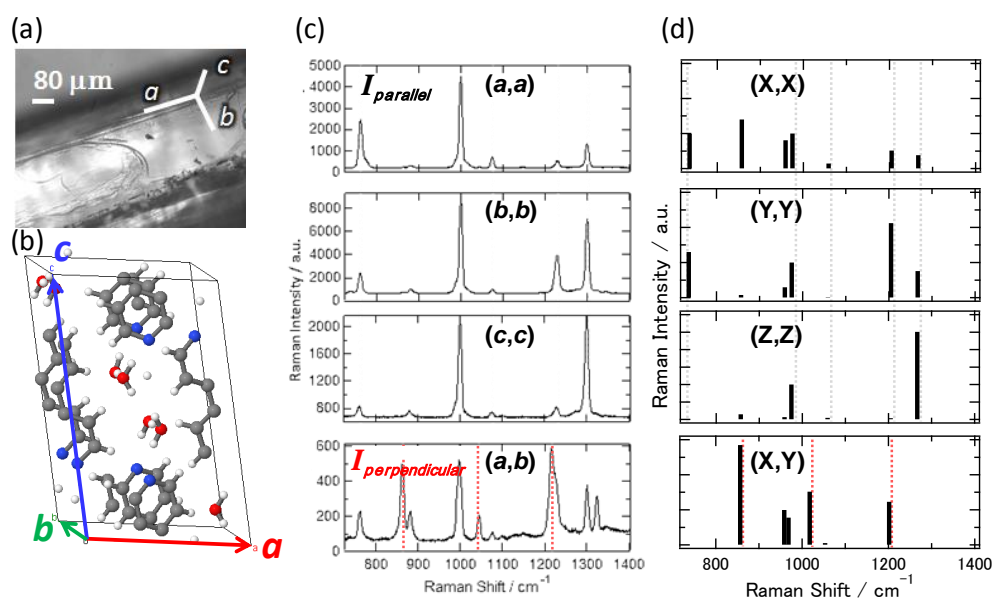

Figure 2.3 Photograph of 4,4'-bipyridine single crystal (a), crystal axis of 4,4'-bipyridine single crystal (b), Polarized Raman spectrum of single crystal at parallel configuration and perpendicular configuration (c). incident and scattering polarization axis were shown in the notation (incident polarization , scattering polarization), calculated polarized Raman spectrum of parallel and perpendicular polarization (d).

30 nm. Gap size are estimated by comparison of the calculation[21]. From the extinction spectra at Fig. 2.4 (b), the polarized excitation along the long axis leads to the appearance of a peak at longer wavelength (around 800 nm). This agrees well with the theoretically calculated spectra of "tip-to-side" Ag triangular dimers whose distances are a few nanometers. So the AR-NSL dimers has a few nanometers gap distance. The spot size irradiated to substrate is estimated ~1 μm, and this area include about 9-10 dimers. This substrate immersed in aqueous solution containing 1 mM 4,4'-bipyridine showed an intense SERS[15]. Polarized SERS measurements on the Ag dimmers at excitation parallel to the dimer axis exhibited well-defined polarization behavior (Fig. 2.4 (c) and (d)). The SERS spectrum at the parallel polarization configuration along the long dimer axis excitation showed intense SERS peaks at 770, 871, 1016, 1074, 1231 and 1296 cm^{-1} (Fig. 2.4 (c)). The observed SERS peaks at the parallel polarization configuration can be assigned to totally symmetric a modes of 4,4'-bipyridine. These peaks were not observed for the measurement on the
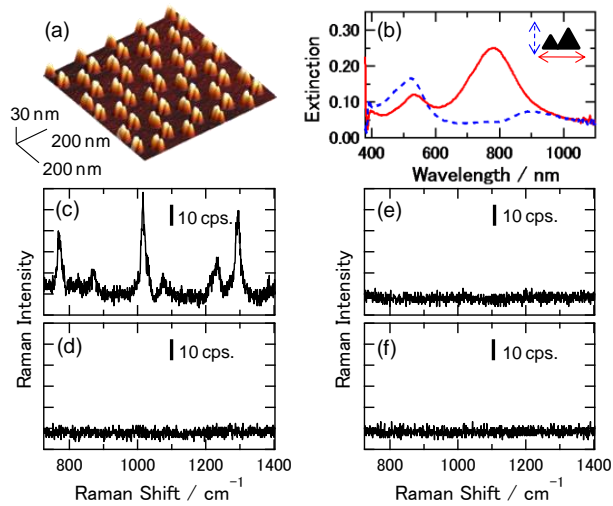

Figure 2.4 AFM image (a), polarized extinction spectrum of Ag nano-dimer array (b), and SERS spectra observed in a 1 mM 4,4'-bipyridine aqueous solution at parallel (c) and perpendicular (d) polarization configuration with parallel excitation to the dimer axis, and parallel (e) and perpendicular (f) configuration with perpendicular excitation to the dimer axis (I_{ex} = 10 mM, t_{ex} = 1s).

scattering at the perpendicular configuration to the long dimer axis (Fig. 2.4 (d)). At the perpendicular excitation to the dimer axis, scattering was not observed at either the parallel or the perpendicular configurations (Fig. 2.4 (e) and (f)).

This apparent difference between the polarization directions at the excitation proves the contribution of the localized electromagnetic field at the gap of the dimers. The present system showed unique behavior in which the polarization of the scattering was dependent upon the SERS active site and the concentration of the solution. Fig. 2.5 depicts polarized SERS spectra observed in 1 mM and 1 mM 4,4' - bipyridine solutions at distinct SERS active sites under excitation parallel to the long dimer axis. At site A, perpendicular polarized scattering was not observed as in the case shown in Fig. 2.4. Increasing the concentration to 1 mM at the same site also resulted in no perpendicular scattering (Fig. 2.5(b)). At site B, relatively weak perpendicular scattering was observed both in 1 μM and 1 mM solutions (Fig. 2.5 (c) and (d)). The perpendicular scattering became much more apparent at site C (Fig. 2.5 (e) and (f)). For the 1 mM solution (Fig. 2.5 (e)), perpendicular polarized scattering was observed with comparable intensity to the parallel polarization. For the 1 mM solution (Fig. 2.5(f)), perpendicular polarized scattering was weak as in the case of site B. It should be noted that all of the observations in Fig. 2.5 were carried out before and after the confirmation that no SERS signal was observed with the excitation of perpendicular polarization to the long dimer axis at the same site. Spectral features were also dependent upon the orientation. Differences in the relative intensities between the bands and the wavenumbers should reflect the orientation of molecules relative to the localized electromagnetic field at the gap part of the dimer. Anisotropy of the highly localized electromagnetic field at the gap leads to a sensitive response in the intensity of the SERS band[22-24]. To discuss the orientation of molecules on the surface, spectral features were compared with those predicted by DFT calculation. SERS spectra at site A exhibited relatively intense bands at 770 and 871 cm^{-1} assigned to the out-of-plane ring and

C–H deformation modes, relatively. These features were reproduced in DFT calculations for the polarization in the X-direction for both excitation and scattering (middle of Fig. 2.5 (a) and (b)). Relatively strong out-of-plane modes vs. the in-plane modes could be attributable to the ''flat'' adsorption of 4,4'-bipyridine rings on the Ag surface.

A localized electromagnetic field perpendicular to the bipyridine rings on the surface may enhance the relative intensity of the band. At site B, the SERS spectrum observed at 1 mM showed a
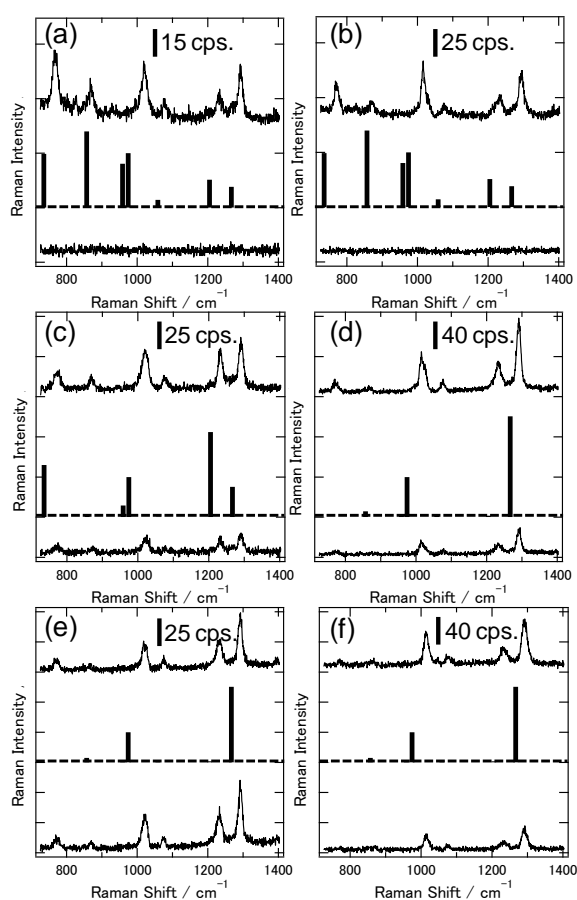

Figure 2.5 SERS spectra observed in 1 mM (a, c, e) and 1 mM (b, d, f) 4,4'-bipyridine aqueous solutions observed at site A (a, b), site B (c, d) and site C (e, f) at the parallel (upper) and perpendicular (lower) polarization configuration with excitation parallel to the dimer axis (I_{ex} = 10 mW, t_{ex} = 1 s); DFT calculation (middle) for polarization of X-excitation and X-scattering (a, b), Y-excitation and Y-scattering (c, d), Z-excitation and Z-scattering directions (d, e, f).

sharp increase in the relative intensity of the band at 1240 cm^{-1} (Fig. 2.5 (c)). At 1 mM, evolution of

the band at 1296 cm^{-1} was observed (Fig. 2.5 (d)). DFT calculations suggested that the band at 1240

cm^{-1} assigned to the in-plane C–H bending mode becomes intense at the ''flat'' adsorption in which

the Y-axis of the molecule is normal to the metal surface. An intense band observed at 1300 cm^{-1}

assigned to the inter-ring stretching mode could be attributed to the ''standing'' adsorption in which

the molecular Z-axis is normal to the surface. The features at site C were comparable to that of site B

in 1 mM solutions. The present band analysis proves the site dependence of the molecular

orientation in the present system.

Relative intensities of the perpendicular to the parallel scattering in site C of Figure 2.5

were plotted as a function of the 4,4'-bipyridine solution concentration in Fig. 2.6. The perpendicular

scattering, i.e., the highly depolarized behavior on SERS, was observed especially at low

concentration. The depolarization was observed when the spectral features corresponded to the

''flat'' adsorption. To evaluate the orientation effect, we plotted the relative intensity against the

Raman intensity ratio of $I_{780cm^{-1}} / I_{1000cm^{-1}}$ and $I_{1300cm^{-1}} / I_{1000cm^{-1}}$ in Figure 2.7. As shown in DFT

calculation, the "flat" adsorption of 4,4'-bipyridine rings on the Ag surface indicate an intense band

at 780 cm^{-1} and "standing" adsorption in which the Y-axis of the molecule is normal to the metal

surface indicate an intense band at 1300 cm^{-1}. These correlation provide that the intense $I_{780cm^{-1}} /$

$I_{1000cm^{-1}}$ corresponds to the "flat" adsorption and intense $I_{1300cm^{-1}} / I_{1000cm^{-1}}$ corresponds to the

"standing" adsorption. "Flat" adsorption tends to have the low relative intensity in Figure 2.7(a). On

the other hand, ''standing'' adsorption indicates the high relative intensity in Figure 2.7 (b). The

present observation of the depolarization behavior clearly demonstrated that orientation of molecules

at the gap affected the polarization of the scattering process. Polarized dependence of SERS has been

discussed with respect to the individual tensors for the excitation field and the scattering field[7, 11]. To

explain the present observation on the depolarization of the scattering photons, selective contributions to the scattering process should be considered. One of the possible contributions is the different two resonance modes of LSPR related with incident and scattering seperately[11].

The extinction of the Ag dimer at longer wavelength region >850 nm in perpendicular polarization contributes to the resonance at perpendicular polarization of the Raman scattering around 1300 cm^{-1} (874 nm). This perpendicular polarization as well as the non-diagonal terms in polarizability tensor which depend on the orientation of adsorbed molecules could induce the perpendicular scattering. This process, however, is not adequate to explain the present observation, because of relatively small intensities of the extinction of the metal structure and the non-totally symmetric bands of a single crystal. Another possibility is that the scattering depolarization observed in the present system could be induced by the resonance of the scattering photons with the localized electronic states caused by the specific adsorption. In the present system, 4,4'-bipyridine molecules adsorbed on the metal surface tend to have the ''standing'' structure when the concentration is more than a few tens of mM due to the coordination ability of the nitrogen atom and the intermolecular
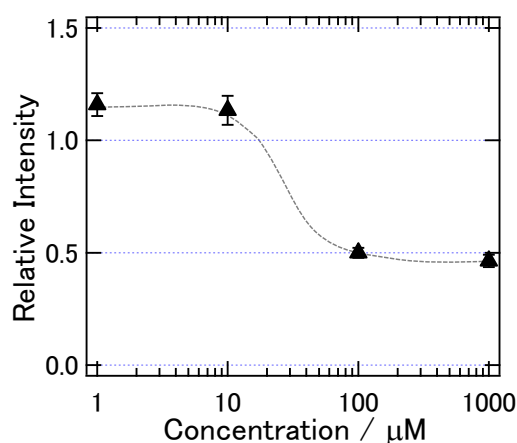

Figure 2.6 Relative SERS intensity ratio of the perpendicular and the parallel polarization configuration with parallel excitation to the dimer axis at various 4,4'-bipyridine concentrations (site C).

interaction[25, 26]. Specific adsorption of molecules could lead to the formation of localized electronic states at the molecule and metal interface. The contribution of the localized resonance states to the SERS process has been considered as the excitation process involving the charge-transfer (CT) contribution, the so-called chemical effect, leading to the observation of non-totally symmetric modes[26]. Although observed bands in the SERS spectra in the present system were fully assigned to totally symmetric modes, characteristics of the SERS spectral features, such as relatively intense bands at 1229 and 1298 cm^{-1} compared with those in bulk solution and a single crystal, could imply the CT contribution[17]. To prove the contribution of the resonance of the localized states to the depolarization, further detailed analysis is required using a system showing well-controlled single molecule SERS.
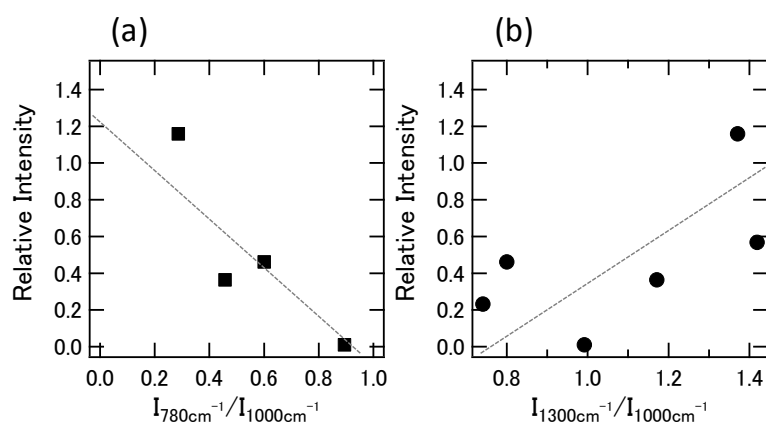

Figure 2.7 Relative intensity ratio of the parallel and perpendicular polarization configuration with parallel excitation to the dimer axis at Raman intensity ratio of $I_{780cm^{-1}}/I_{1000cm^{-1}}$ and $I_{1300cm^{-1}}/I_{1000cm^{-1}}$, all concentration is 1 μM.

2.4 Conclusion

In conclusion, the substrate with a Ag nano-dimer array immersed in 4,4'-bipyridine solution showed depolarized SERS behavior depending on the adsorbed structure of molecules at the gaps of the dimer. The orientation of molecules was discussed by comparison of SERS spectra with those obtained by conventional polarized Raman spectra of a homogeneous aqueous solution and a single crystal of 4,4'- bipyridine. The SERS depolarization at specific adsorption states of molecules implies that the molecule and metal interface modulate the scattering polarization selectively.

2.5 References

1.   Moskovits, M.; Suh, J. S. *J. Phys. Chem.* **1984,** 88, 1293-1298.

2.   Sano, H.; Mizutani, G.; Ushioda, S. *Phys. Rev. B* **1993,** 47, 13773-13781.

3.   Bosnick, K. A.; Jiang; Brus, L. E. *J. Phys. Chem. B* **2002,** 106, 8096-8099.

4.   Jiang; Bosnick, K.; Maillard, M.; Brus, L. *J. Phys. Chem. B* **2003,** 107, 9964-9972.

5.   Xu, H.; Kall, M. *Chemphyschem* **2003,** 4, 1001-5.

6.   Shegai, T. O.; Haran, G. *J. Phys. Chem. B* **2006,** 110, 2459-2461.

7.   Shegai, T.; Li, Z.; Dadosh, T.; Zhang, Z.; Xu, H.; Haran, G. *Proc. Natl. Acad. Sci. USA* **2008,** 105, 16448-16453.

8.   Li, Z.; Shegai, T.; Haran, G.; Xu, H. *ACS Nano* **2009,** 3, 637-642.

9.   Le Ru, E. C.; Etchegoin, P. G. *Chem. Phys. Lett.* **2006,** 423, 63-66.

10.   Le Ru, E. C.; Meyer, M.; Blackie, E.; Etchegoin, P. G. *J. Raman Spectrosc.* **2008,** 39, 1127-1134.

11.   Le Ru, E. C.; Grand, J.; Félidj, N.; Aubard, J.; Lévi, G.; Hohenau, A.; Krenn, J. R.; Blackie, E.; Etchegoin, P. G. *J. Phys. Chem. C* **2008,** 112, 8117-8121.

12.   Moroz, A. *J. Opt. Soc. Am. B* **2009,** 26, 517-527.

13.   Jernshøj, K. D.; Hassing, S. *J. Raman Spectrosc.* **2010,** 41, 727-738.

14.   Yoshida, K.-i.; Itoh, T.; Biju, V.; Ishikawa, M.; Ozaki, Y. *Phys. Rev. B* **2009,** 79, 085419.

15.   Sawai, Y.; Takimoto, B.; Nabika, H.; Ajito, K.; Murakoshi, K. *J. Am. Chem. Soc.* **2007,** 129, 1658-1662.

16.   Fischer, U. C.; Zingsheim, H. P. *J. Vacuum Sci. & amp; Tech.* **1981,** 19, 881-885.

17.   Lim, J. K.; Joo, S.-W. *Surface and Interface Analysis* **2007,** 39, 684-690.

18.   Topaçli, A.; Akyüz, S. *Spectrochimica Acta Part A: Molecular and Biomolecular Spectroscopy* **1995,** 51, 633-641.

19.   Kamyshny, A. L.; Zakharov, V. N.; Fedorov, Y. V.; Galashin, A. E.; Aslanov, L. A. *J. Colloid and Interface Sci.* **1993,** 158, 171-182.

20.   Näther, C.; Riedel, J.; Jeß, I. *Acta Crystallographica Section C* **2001,** 57, 111-112.

21.   Hao, E.; Schatz, G. C. *J. Chem. Phys.* **2004,** 120, 357-366.

22.   Battisti, D.; Aroca, R.; Loutfy, R. O. *Chem. Mat.* **1989,** 1, 124-128.

23.   Gucciardi, P. G.; Bonaccorso, F.; Lopes, M.; Billot, L.; de la Chapelle, M. L. *Thin Solid Films* **2008,** 516, 8064-8072.

24.   Uosaki, K.; Allen, H.; Hill, O. *J. Electroanal. Chem. Interfacial Electrochem.* **1981,** 122, 321-326.

25.   Yang, D.; Bizzotto, D.; Lipkowski, J.; Pettinger, B.; Mirwald, S. *J. Phys. Chem.* **1994,** 98, 7083-7089.

26.   Lombardi, J. R.; Birke, R. L. *Accs.Chem. Res.* **2009,** 42, 734-742.

Simultaneous Measurement of

Surface-Enhanced Raman Scattering and Conductance

using Mechanically Controllable Break Junction Technique

3.1 Introduction

In Chapter 2, I analyzed the depolarization behavior of SERS at metal nano-gap structure. Depolarization is strongly dependent on the adsorbed structure of the metal surface. Ensemble measurement of the adsorbed molecules and each metal structure show the fluctuation in the depolarization SERS behavior and the intensity ratio in the same spectrum. For further investigation about depolarization behavior it is important to fabricate single molecular junction combined with a spectroscopy of the single molecule. Up to now, vibrational spectroscopy about single molecule was investigated in the field of the adsorbed molecules. In 1998, first observation about acetylene molecule was performed by using scanning tunneling microscopy (STM)[1]. Then inelastic tunneling microscopy[2-5] and single molecular fluorescence[6] and STM light emission spectra which has vibrational-induced tructures[7] were measured for investigating single molecular vibrational spectroscopy.

Single metal atomic contact shows the specific conductance limited by the density of the electronic states characterized by free electron metals. In the case of Au, STM show the 1 G_0 (= 12.9 Ω^{-1}) at the metallic nano-wire of the single atom conductatnce[8-12]. The Au nano-wire shows the quantized conductance at metallic junction. In the same time of the formation of the 1 G_0

conductance, single atom contact was measured by using ultrahigh-vacuum electron microscope[9].

The quantized conductance in a confined small area of metal is shown as (3.1).

$$G = n\left(\frac{2e^2}{h}\right) = nG_0 \quad (n = 1, 2, 3 \cdots) \quad\quad (3.1)$$

Where e is the electron charge, h is Planck's constant, $G_0 = 2e^2/h = (12.9\,k\Omega)^{-1}$ is a unit

of quantum conductance and n is number of electronic state concerned about the conductance. More

general condition, the conductance of the metal atomic contact is expressed by the Landaur

formula[13] as described in (3.2).

$$G = \left(\frac{2e^2}{h}\right)\sum_i^n T_i = G_0 \sum_i^n T_i \quad (n = 1, 2, 3 \cdots) \quad\quad (3.2)$$

Where T_i is the transmission probability of the i-th conductance channel. Conduction electron is

affected by the scattering when the transmittance in the metallic nano-junction. T_i denotes the

transmission probability in the process of the scattering. If this junction is immersed in the solution

of some molecules, the adsorbed molecule combined to the gap of the junction in the process of the

breaking. Then conductance of metal / molecule / metal junction is measured. The system which

cause single molecular junction at the metal nano-dimer structure show the intrinsic conductance

properties at the metal junction. If there are no intermolecular interaction, conductance is originated

from the addition of the conductance from consisted molecules. In other words, when the

conductance is changing by integral multiple, the smallest conductance unit indicates the formation

of the single molecular junction.

In the junction, two facing triangle like nano-structure show the intense electromagnetic

field between the gap of junction by localized surface plasmon resonance. The intense

electromagnetic field becomes possible to measure surface-enhanced Raman scattering in

metal/molecule/metal junction. Until now, there are measurements which are performed at the single molecule junction[14-17]. These systems had the high sensitivity about the single molecule detection owing to LSPRs. However detailed feature about the intensity ratio of the Raman spectrum scarcely analyze about molecular structure. Moreover it is expected that polarized Raman measurement also proves the charge transfer character in the molecule / metal interface.

In this chapter simultaneous measurement of conductance and polarized surface-enhanced Raman scattering about the molecular bridged metal nano junction were performed. Conductance measurement proves the number of molecules and polarized Raman measurement proves the orientation and charge transfer character.

3.2 Experimental

The mechanically controllable break junction (MCBJ) sample was fabricated using electron-beam lithography (Figure 3.1 (b)). The bending substrate was a plate of Al about 0.8 mm thick, 22 mm long and 11 mm wide. The 200 nm thick Al_2O_3 film was formed on the Al plate by the anodic oxidation method. The oxide film (Al_2O_3) was used as an insulating film, because the background of the Raman spectrum can be reduced as compared to the system using organic insulating film. On this substrate, a polyimide layer was spin-coated with a thickness of 600 nm. The Au nanoelectrode was patterned on the substrate using electron beam lithography and lift-off technique. Au (120 nm) and Cr (1 nm) were deposited with the electron beam evaporation technique. Subsequently, the polyimide underneath the Au nanoelectrode was removed by reactive ion etching using O_2/CF_4 plasma. A free-standing Au nanobridge was obtained. The whole assembly was mounted on a three-point bending mechanism, consisting of a stacked piezo-element (NEC tokin) and two fixed counter supports. The water solution containing 1 mM 4,4'-bipyridine was dropped

onto the Au nanobridge. By bending the substrate, the top surface of the substrate was expanded, and the Au nano bridge finally broke, forming a molecular junction in solution. By relaxing the bending of the substrate, the Au nanobridge could be re-established. The conductance measurement was carried out with 20 mV bias voltage and sampling rate was 1000 plot/sec/.

SERS measurement was performed using a home-made polarized Raman microprobe spectrometer. Excitation energy is 785 nm (1.58 eV) and excitation power is 0.2 mW. Raman measurement were carried out at the backscattering configuration collected the scattering phtons with the parallel and perpendicular polarization directions simultaneously. The expanded NIR beam is focused onto the sample using a water-immersion objective lens with 100x magnification and a numerical aperture of 1.0 (Figure 3.1 (a)). Raman image measurement was carried out by imaging Raman scattering at the excitation using an expanded NIR laser beam with a diameter of approximately 30 μm.

Raman spectra simulation were carried out using Gaussian 03, revision E.01, at the B3LYP level of DFT with LanL2DZ basis set for Au atoms and 6-31 G** basis sets for other atoms. The $(Au)_2$ cluster was used in the calculations as a model of gold substrates. The vibration symmetry type is described by using D_2 symmetry of 4,4'-bipyridine molecule.
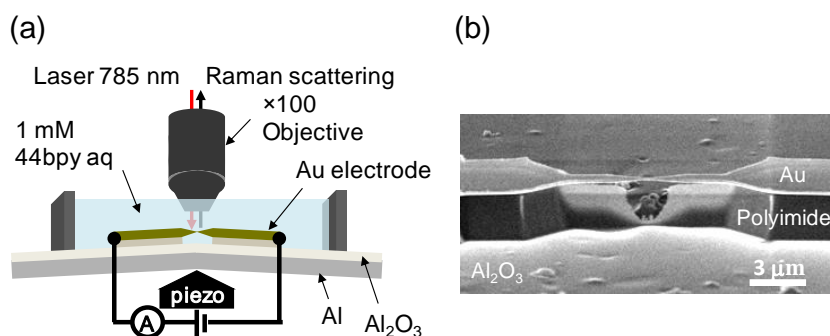

Figure 3.1. measurement system of the simultaneous measurement of Raman and single molecule conductantce (a) and gap structure image by scanning electron microscope (b).

3.3 Results and Discussion

Figure 3.2 shows the Conductance trace of signle metal nanojunction at single atomic junction region during breaking process of the contact. This trace shows the stepwise decrease about the time course. In this region, Plateau of 1 G_0 is corresponding to single atomic contact[8-12]. Then 2 G_0 and 3 G_0 trace indicate the two and three Au atoms at the gap of Au junction. The Au junction immersed in 1 mM 4,4'-bipyridine aqueous solution show the not only 1 G_0 trace but also 0.01 G_0 trace in the process of break of junction. Previously documented conductance ranges from 1.6×10^{-4} G_0 to 0.01 G_0[17-21]. The wide range may be due to differing experimental conditions (e.g., solvent, concentrations, bias voltage, and sample treatment). I investigated the conductance of the single 4,4'-bipyridine molecule junction using a scanning tunneling microscope (STM) break junction technique under the same experimental conditions as those for the SERS measurements. Observation of conductance indicates formation of a single molecule junction. In the present study, I observed significant modulations in both SERS intensity and the selectivity of the Raman vibrational bands that were coincident with current fluctuations in the single 4,4'-bipyridine molecule junction. Figure
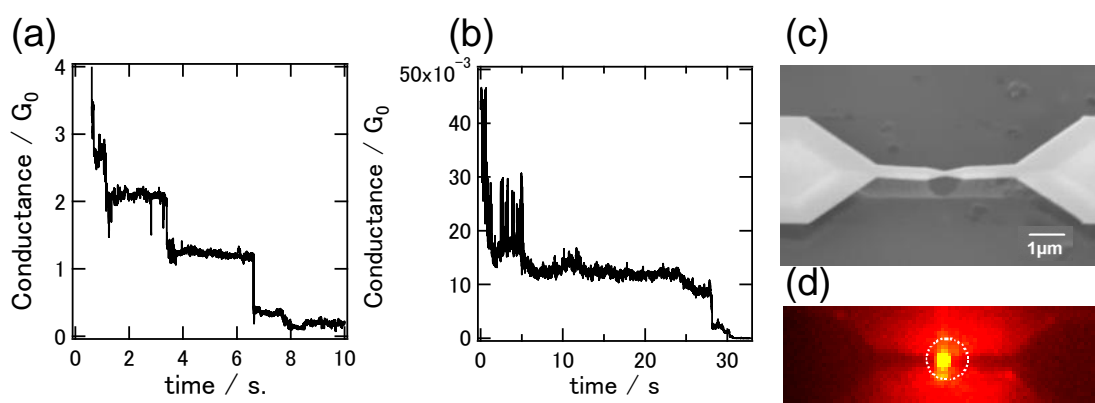

Figure 3.2 Conductance trace of the 1 G_0 area (a), 0.01 G_0 area (b), SEM image (c), Raman image at 1018 cm^{-1} (d).

3.2 (c) show the scanning electron microscope image of substrate. In the plateau of 0.01 G_0 Raman image at C-H vibrational mode (1018 cm^{-1}) were obtained in Figure 3.2 (d). It reveals that the gap of the junction is main enhanced area.

Figure 3.3 (a) shows the time course of the conductance around 0.01 G_0. Fluctuation of the conductance between 0.005 G_0 and 0.01 G_0 were observed. Lower conductance than 0.01 G_0 indicates the weak adsorption of the molecular bridging structure. Then, time course of conductance represents the switching between strong (1 - 6 s, 14 - 20 s) and weak adsorption strength (7 - 13 s). Simultaneously Raman spectra were acquired (Figure 3.3(b)). The strong and obvious Raman modes were measured all of time range. The additional Raman mode were measured in the higher conductance (= 0.01 G_0) region. Figure 3.3 (c, top) shows typical Raman spectra in the region of
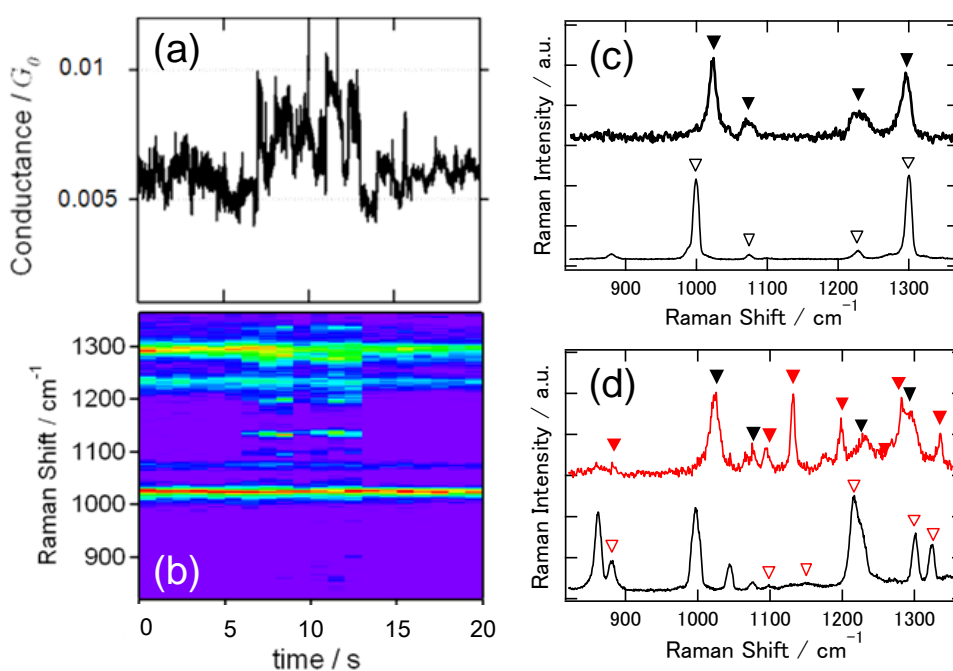

Figure 3.3 Simultaneous measurement of conductance(a) and Raman spectra (b), Raman spectra of conductance < 0.01 G_0 region (c, top) and polarized Raman spectrum of 4,4'-bipyridine single crystal (c, bottom), conductance = 0.01 G_0 (d, top) and polarized Raman spectrum (d, bottom).

41

lower conductance (< 0.01 G_0). Raman peak at 1015, 1074, 1230, 1297 cm^{-1} were measured (solid black arrows). Corresponding Raman mode were parallel polarization molecular spectra in Figure 3.3 (c, bottom). These peaks were assigned totally symmetric a mode. Figure 3.3 (d, top) shows typical Raman spectra in the region of higher conductance ($= 0.01$ G_0). Additional Raman peak at 880, 1095, 1132, 1198, 1282, 1330 cm^{-1} were measured (solid red arrows). Additional peaks were assigned nontotally symmetric b_1 mode. This additional non-totally symmetric mode appearanece are not explained by the electromagnetic field enhancement. As already shown in Chapter 2, it is predicted that non-totally symmetric mode were enhanced by the charge transfer mechanism for SERS.

Charge transfer mechanism is the resonant Raman like enhancement. In this case I have to consider about the energy state of the Au Fermi level and highest occupied molecular orbital (HOMO) and lowest unoccupied molecular orbital (LUMO) of 4,4'-bipyridine molecule. When 4,4'-bipyridine molecules are bridged to the Au junction, hybridization between metal and molecule change the LUMO (B$_3$ symmetry) energy to close to Fermi level[22]

Figure 3.4 Energy diagram of the resonant condition in the high conductance region.

(Figure 3.4). In present case, it is suggested that charge transfer from metal to LUMO is resonant to excitation energy. This energy level provides the x-direction induced dipole moment which is vertical to pyridine rings. In the CT mechanism, term C in the model of Lombardi et al. represented by eq. (1. 18, 1. 22)[23].
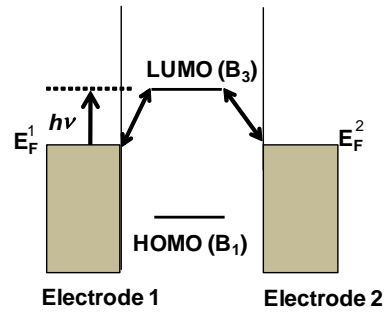
$$\alpha_{\rho\sigma} = A_f + A_k + B + C \qquad (1.18)$$

$$C = -\frac{2}{\hbar} \sum_{K \neq I} \sum_{M > I} M_{MK}^{\sigma} M_{KI}^{\rho} h_{IM} \langle i | Q | f \rangle \frac{\left(\omega_{KI} \omega_{KM} + \omega^2 \right)}{\left(\omega_{KI}^2 - \omega^2 \right)\left(\omega_{KM}^2 - \omega^2 \right)} \qquad (1.22)$$

esonant condition is predicted when $\omega \approx \omega_{KM}$. For the C-term to be nonvanishing, $\langle i|Q|f \rangle$ must be nonzero. In the fundamental mode, usual selection rule become $f = i \pm 1$. In addition, it is required for C that neither h_{IK} nor components of M_{MK} and M_{KI} vanish. From the intensity borrowing the $I{\rightarrow}K$ transition, vibrational mode can be arrowed. Allowed Raman mode by CT was described in table 3.1 at each direction of charge transfer, that is, adsorption orientation.

In the present system, the *a*-mode enhancement was measured in the lower conductance region. Totally symmetric a-mode is predicted by the electromagnetic field enhancement. If CT resonance is affected additionally, x-directed adsorbed orientation, that is flat adsorption on the metal surface, is expected. The intensity ratio of Raman spectrum predicted the z-directed adsorbed orientation in the junction. Therefore a-mode vibrational mode is induced by EM effect. On the other hand, *a*-mode and *b₁*-mode were coincidentally generated in the higher conductance region. The appearance of b1-mode is expected to be produced in the y-directed adsorbed orientation by CT mechanism (Table 3.1). Conductance shows the fluctuation of the junction from the breaking to the formation. Inclined orientation of the molecules situated in the gap provides the charge transfer between molecule and metal surface.

Table 3.1 enhanced Raman mode selection rule by charge transfer mechanism.

Symmetry of LUMO	Induced dipole moment	Adsorbed orientation	Enhanced vibrational mode
B_3	$\mu_x(X)$	X	$a\,(\alpha_{xx}\,\alpha_{yy}\,\alpha_{zz})$
		Y	$b_1\,(\alpha_{xy})$
		Z	$b_2\,(\alpha_{xz})$
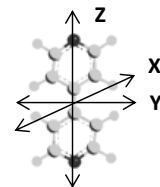
3.4 Conclusion

In this chapter, I have successfully fabricated the single molecular environment for measuring the Raman scattering which is possible to measure the conductance simultaneously. The conductance measurement clarifies the number of molecules between the junction and strength of adsorption. Moreover Raman measurement reveals presence of the charge transfer from molecules to metal. Charge transfer process provides the additional electronic resonant condition. The modulation of small fraction of the adsorption structure at the interface strongly affect to the process of the electric excitation.

3.5 References

1.   Stipe, B. C.; Rezaei, M. A.; Ho, W. *Science* **1998,** 280, 1732-1735.

2.   Smit, R. H. M.; Noat, Y.; Untiedt, C.; Lang, N. D.; van, H. M. C.; van, R. J. M. *Nature* **2002,** 419, 906-909.

3.   Troisi, A.; Ratner, M. A. *Nano Lett.* **2006,** 6, 1784-1788.

4.   Hihath, J.; Arroyo, C. R.; Rubio-Bollinger, G.; Tao, N.; Agraït, N. s. *Nano Lett.* **2008,** 8, 1673-1678.

5.   Kiguchi, M.; Tal, O.; Wohlthat, S.; Pauly, F.; Krieger, M.; Djukic, D.; Cuevas, J. C.; van, R. J. M. *Phys. Rev. Lett.* **2008,** 101, 046801.

6.   Qiu, X. H.; Nazin, G. V.; Ho, W. *Science* **2003,** 299, 542-546.

7.   Uehara, Y.; Ushioda, S. *Surf. Sci.* **2007,** 601, 5643-5648.

8.   Pascual, J. I.; Méndez, J.; Gómez-Herrero, J.; Baró, A. M.; García, N.; Binh, V. T. *Phys. Rev. Lett.* **1993,** 71, 1852-1855.

9.   Ohnishi, H.; Kondo, Y.; Takayanagi, K. *Nature* **1998,** 395, 780-783.

10.   Costa-Krämer, J. L.; García, N.; Olin, H. *Phys. Rev. B* **1997,** 55, 12910-12913.

11.   Ludoph, B.; Devoret, M. H.; Esteve, D.; Urbina, C.; van Ruitenbeek, J. M. *Phys. Rev. Lett.* **1999,** 82, 1530-1533.

12.   Hansen, K.; Lægsgaard, E.; Stensgaard, I.; Besenbacher, F. *Phys. Rev. B* **1997,** 56, 2208-2220.

13.   Landauer, R. *IBM J. Res. Dev.* 1, 223.

14. Ward, D. R.; Halas, N. J.; Ciszek, J. W.; Tour, J. M.; Wu, Y.; Nordlander, P.; Natelson, D. *Nano Lett* **2008,** 8, 919-24.

15. Tian, J. H.; Liu, B.; Li, X.; Yang, Z. L.; Ren, B.; Wu, S. T.; Tao, N.; Tian, Z. Q. *J. Am. Chem. Soc.* **2006,** 128, 14748-9.

16. Wang, X.; Liu, Z.; Zhuang, M.-D.; Zhang, H.-M.; Wang, X.; Xie, Z.-X.; Wu, D.-Y.; Ren, B.; Tian, Z.-Q. *Appl. Phys. Lett.* **2007,** 91, 101105/1-101105/3.

17. Liu, Z.; Ding, S.-Y.; Chen, Z.-B.; Wang, X.; Tian, J.-H.; Anema, J. R.; Zhou, X.-S.; Wu, D.-Y.; Mao, B.-W.; Xu, X.; Ren, B.; Tian, Z.-Q. *Nat. Commun.* **2011,** 2, 1310/1-1310/6.

18. Xu, B.; Tao, N. J. *Science* **2003,** 301, 1221-1223.

19. Quek, S. Y.; Kamenetska, M.; Steigerwald, M. L.; Choi, H. J.; Louie, S. G.; Hybertsen, M. S.; Neaton, J. B.; Venkataraman, L. *Nature Nanotechnol.* **2009,** 4, 230-234.

20. Horiguchi, K.; Kurokawa, S.; Sakai, A. *J. Chem. Phys.* **2009,** 131, 104703.

21. Zhou, X.-S.; Chen, Z.-B.; Liu, S.-H.; Jin, S.; Liu, L.; Zhang, H.-M.; Xie, Z.-X.; Jiang, Y.-B.; Mao, B.-W. *J. Phys. Chem. C* **2008,** 112, 3935-3940.

22. Li, Z.; Kosov, D. S. *J. Phys. Chem. B* **2006,** 110, 9893-9898.

23. Lombardi, J. R.; Birke, R. L.; Lu, T.; Xu, J. *J. Chem. Phys.* **1986,** 84, 4174-4180.

Chapter 4

Electronic Excitation of an Isolated Single-Walled Carbon Nanotube by Tuning Electrochemical Potential

4.1 Introduction

Localized surface plasmon resonance (LSPR) is an effective perturbation to transfer the energy of photons to electrons in materials/molecules at the interface. Electronic excitation is very important to control the orientation of the molecules situated in the metal surface and the electronic state at the interface. Single walled carbon nanotube (SWNT) should be a promising tool as a analyte because of its electronic structures well-defined by the geometrical structure characterized by chirality[1, 2]. The density of the electronic states of SWNT, which can be controlled by chemical/electrochemical doping, is also unique measure for the determination of potential diagram of the system.

SWNT has the intrinsic excitation properties[3-13]. A SWNT can be viewed as a strip cut from an infinite graphene sheet that is rolled up seamlessly to form a tube. The chirality determines the diameter and the chiral angle. The diameter and helicity of a SWNT are defined by the roll-up vector $C_h = n\mathbf{a}_1 + m\mathbf{a}_2 \equiv (n,m)$, which connects crystallographically equivalent site on this sheet. $\mathbf{a}_1$ and $\mathbf{a}_2$ are the graphene lattice vectors, and n and m are integers. These structures of SWNT show the individual van Hove singularities in electronic density of states because of the 1D structure of SWNT. Electronic absorption in symmetrical vHS ($\pm E_i$) against the Fermi level is allowed in the parallel absorption to nanotube axis. In the perpendicular polarization the $E_i \rightarrow E_{i\pm1}$ are allowed.

When this E_{ii} transition is resonant with the excitation energy, resonant Raman intensity becomes active. Resonance Raman scattering (RRS) is widely used for the sample evaluation and characterization of carbon nanotubes because it is a noncontact and nondestructive measurement[13-15]. Moreover these techniques can operate at room temperature and in air. The low frequency features (100-400 cm^{-1}) show the radial breathing mode (RBM). This mode is vibration of carbon atoms in a radial direction in relation to the nanotube axis. The graphite-like band (G-band) in carbon nanotubes is directly related to the G-band in graphite that is identified with an in-plane tangential optical phonon involving the stretching of the bond between the two atoms in the graphene unit cell. In the region of 1500 cm^{-1} G-band is measured in the Raman spectrum. Because of the highly asymmetric feature of SWNT, G-band split into 6 bands which is called A^{+}, A^{-}, E_1^{+}, E_1^{-}, E_2^{+}, E_2^{-} modes. These Raman intensity ratios of spectrum are reflected the orientation to the light polarization[16]. In the metal nano-gap which causes the anisotropic electromagnetic field the intensity ratio of the G-band are assigned to the direction in the gap. From the Raman spectrum I can determin both of the singularity of SWNT and the orientation of the SWNT against the LSPR electromagnetic field direction. In the region of 1300 cm^{-1} D-band is measured which is originated from the disorder-induced mode.

For the purpose of estimation of the SWNTs, electrochemical environment were adopted to modulate the doping density. Bard et al. presented first electrochemical study of a SWNT deposited on Pt or Au electrodes[17]. Then first observation about the individual SWNT was presented in 2005 by Heller et al[18]. In 1997, pioneering redox-doped SWNT Raman investigation were performed (without using electrochemistry)[19]. Raman spectrum of bundle SWNTs were acquired in the electrochemical environment. This measurement was actually provided about the chemical/electrochemical doping. In 2000, Kavan et al. studied electrochemistry in aqueous electrolyte solution[20] and Fischer et al. studied in aprotic electrolyte solution[21]. Absolute potential of

the Fermi level in an isolated nanotube was determined by Okazaki et al[22-24]. It is known that resonant Raman profile reflects the vHSs. SWNTs have the quantum capacitance properties which is observed in the electrochemical environment[17, 18, 25-27]. The character keeps the electronic density of states when the electron filling of the conduction band and depletion of the valence band. Only the Fermi level is tuned in the electrochemical environment[22, 28, 29]. Spectroelectrochemistry especially in Raman measurement provides the fruitful information about SWNT. The frequency of RBM keeps while the tuning of electronic density of state. And the intensity of RBM and G-band are modulated by the depletion / filling of valence / conduction band. The frequency of G-band and D-band are varied by the electrochemical potential. The measurement of Raman scattering combined electrochemistry are supposed to clarify the electronic density of states in the isolated SWNT level[30-32].

For the clarifying the electric excitation behavior in the LSPR induced electromagnetic field, polarized Raman measurement combined the electrochemistry is very important. However the combination of the polarized Raman measurement in the electrochemical environment has not been performed yet. In this chapter, I measured the polarized Raman measurement which was performed in the electrochemical environment by using metal nano-dimer array. By confirming the singularities about the SWNT I analyze the G-band intensity ratios by changing electrochemical potential. Then I analyzed the electronic excitation about the SWNTs.

4.2 Experimental

In the experimental, Au dimer arrays were fabricated on the indium tin oxide glass by an angle-resolved nanosphere lithography technique (AR-NSL) as a working electrode. The sample of carbon nanotubes were prepared by alcohol catalytic chemical vapor deposition method. The sample

of SWNT was mono-dispersed in the N-methyl-2-pyrrolidone solution. The individual SWNT on the Au-NSL surface was conducted by dropwise introduction. Polarized Raman measurement (λ_{ex} = 785 nm) was acquired in the back scattering configuration by using immersion lens ($\times$100) under electrochemical potential control. The aprotic electrolyte of ionic liquid of TMPA-TFSA (N,N,N-trimethyl-N-propylammoniumubis (trifluoromethanesulfonul) amide) was used in the electrochemical measurement. The solution was dehydrated overnight at $110^\circ C$. Then the sample was situated in vacuum oven overnight for deoxidation. The reference electrode was Ag/0.05 M Ag$^+$ TMPA-TFSA (4.92 V vs. vacuum level) and the counter electrode was Pt plate.

4.3 Results and Discussion

Figure 4.1(a) shows the typical resonant Raman spectrum (excitation wavelength λ_{ex} = 785 nm). In the region of the 100-300 cm^{-1} these mode are assigned to the RBM. Figure 4.1 (b) shows the typical Surface-enhanced resonant Raman spectrum at the metal nano-gap. The single RBM mode
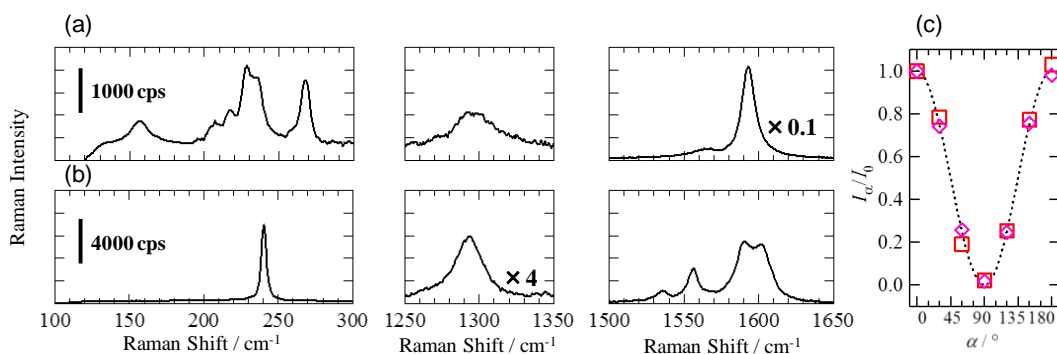

Figure 4.1 Resonant Raman scattering spectrum (a) and surface-enhanced resonant Raman scattering (SERRS) spectrum (b) and SERRS intensity profile as a function of incident polarization angle to the dimer long axis (c). Excitation power I_{ex} = 2 mW (a) and I_{ex} = 0.2 mW (b). exposure time t_{ex} = 100 s (a), exposure time t_{ex} = 1 s (b).

obtained at 241 cm^{-1} is assigned (8, 6) semiconducting nanotube. Figure 4.1 (c) shows the Raman intensity profile as a function of incident polarization angle to the dimer long axis. The dotted line presents $\cos^2\alpha$ correlation which is concerned about the LSPR electromagnetic field correlation. This represents the SWNT affected the electromagnetic field of LSPR in the gap. Then it is found that the SERRS measurement of isolated SWNT was achieved.

Surface-enhanced Raman scattering at each polarized configuration were acquired (Figure 4.2 (a, b)). RBM mode were obtained at ω_{RBM} = 228 cm^{-1} and ω_{RBM} = 233 cm^{-1}. Both are assigned to semiconducting nanotubes. In Figure 4.2 (a) G-bands are acquired in 1538 cm^{-1} (E_2^-), 1558 cm^{-1} (A^-), 1591 cm^{-1} (A^+), 1603 cm^{-1} (E_2^+) at parallel polarization configuration (red solid line) and 1567 cm^{-1} (E_1^-), 1594 cm^{-1} (E_1^+) at perpendicular polarization configuration (blue solid line). At the polarized Raman activity correlation at each incident polarization angle (α) in Figure 4.2 (a, right side) A and E_2 mode are obtained without E_1 mode at α = 90° against the dimer long axis. In the parallel
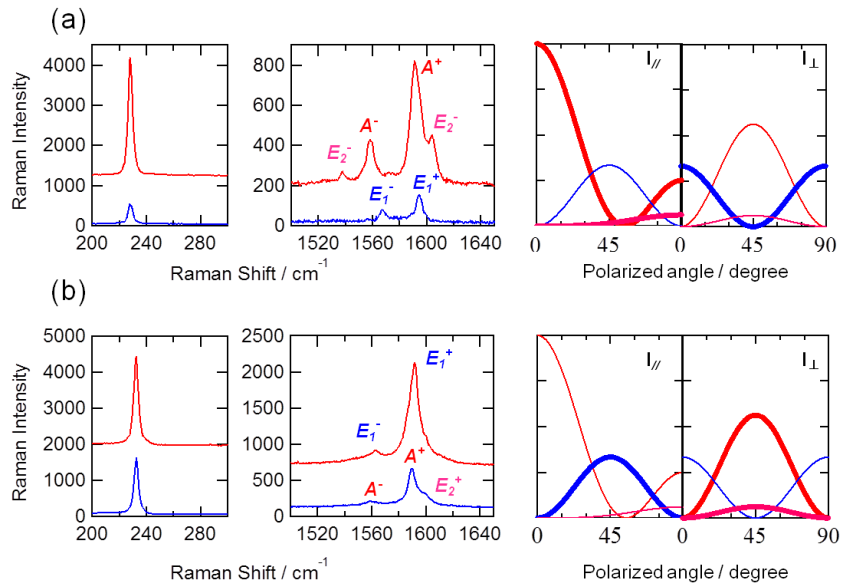

Figure 4.2 Polarized Raman spectra of different site, Excitation power I_{ex} = 0.2 mW, exposure time t_{ex} = 1 s . ω_{RBM} = 228 cm^{-1}, d = 1.04 nm, semiconducting (10, 5) nanotube (a) and ω_{RBM} = 233 cm^{-1}, d = 1.00 nm, semiconducting (11, 3) nanotube (b).

polarization configuration at $\alpha = 90°$ only E_1 mode is observable. In a similar fashion, Figure 4.2 (b)

shows that G-band are acquired in 1564 cm^{-1} (E_1^-), 1593 cm^{-1} (E_1^+) at parallel polarization

configuration and 1560 cm^{-1} (A^-), 1591 cm^{-1} (A^+), 1600 cm^{-1} (E_2^+) at perpendicular polarization

configuration. This mode appearance at each polarization configuration shows the $\alpha = 45°$ at the

nano-gap. The A and E_2 mode are observed in the parallel transition to nanotube axis and E_1 mode is

observed in the parallel transition. Polarized Raman spectrum of SWNT is proved the anisotropic

transition about the nanotube axis. The purpose of comparing to resonance Raman and

surface-enhacned resonance Raman scattering I obtained in the same condition of chirality and
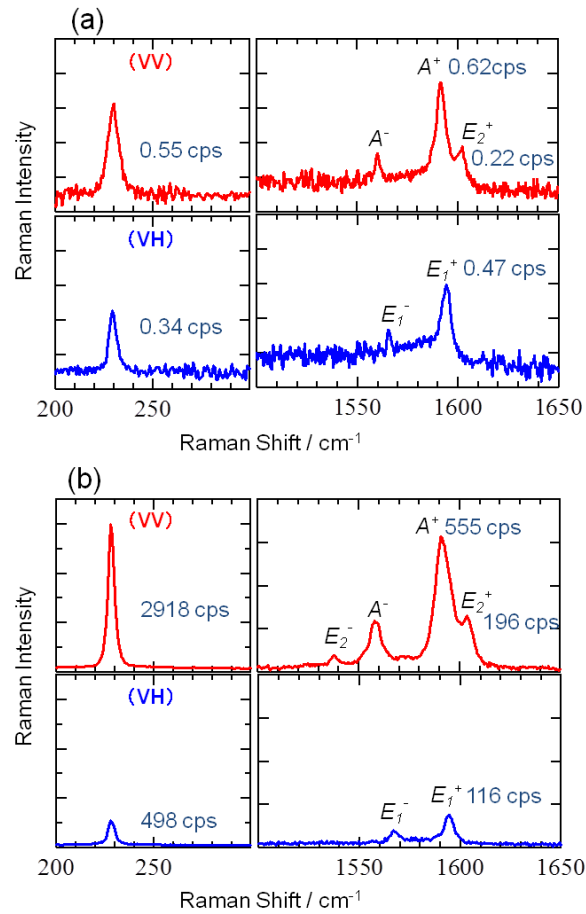

Figure 4.3 Polarized resonant Raman spectrum (a) and polarized surface-enhanced resonant Raman spectrum (b). $\omega_{RBM} = 228$ cm^{-1}, d = 1.04 nm, semiconducting (10, 5) nanotube (a, b).

polarization angle α. Figure 4.2 (a, b) are $\omega_{RBM} = 233$ cm^{-1}, then (11, 3) semiconducting nanotube (d = 1.00 nm). The intensity is affected by the signal enhancement at each configuration. The resonant Raman scattering showed the G-band in 1558 cm^{-1} (A$^-$), 1591 cm^{-1} (A$^+$), 1603 cm^{-1} (E$_2^+$) at parallel polarization configuration (red solid line) and 1567 cm^{-1} (E$_1^-$), 1594 cm^{-1} (E$_1^+$) at perpendicular polarization configuration (blue solid line), same as SERRS (Figure 4.3 (b)). The intensity ratio of these G-band feature indicates the α = 45° against the tube axis. The SERRS spectrum shows the similar depolarization feature to the resonant Raman spectra. In the resonant condition with the LSPRs, SERRS spectra show the intense Raman scattering because of two-fold enhancement mechanism. The enhancement are appeared in the parallel polarization configuration to the LSPR direction. Though the perpendicuclar polarization configuration hardly provides the enhancement,
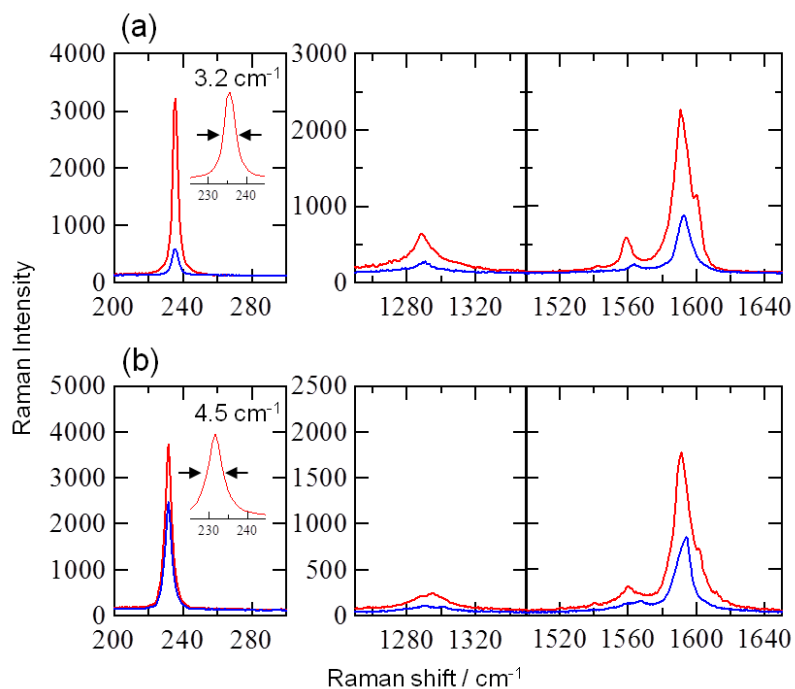

Figure 4.4 Polarized resonant Raman spectra at different site: parallel polarization configuration (red line) and perpendicular polarization configuration (blue line). $\omega_{RBM} = 228$ cm^{-1}, d = 1.04 nm, semiconducting (11, 3) nanotube (a, b).

polarized SERRS spectrum shows the some enhanced signal. This feature was examined by the intensity ratio between RRS and SERS. From the intensity ratio at parallel polarization configuration between, in addition to the confinement of the enhanced field $\sim 10^{3\text{-}4}$, the enhancement factor at incident and scattering polarization was estimated about $0.8 - 2.7 \times 10^3$. By using this factor at perpendicular polarization configuration, the intensity ratio between RRS and SERRS become present the additional enhancement ($1.2 - 3.9 \times 10^2$) to the LSPR enhancement only caused in the incident process. The additional enhancement at the perpendicular polarization suggests to be caused by the electronic excitation near the metal surface. Electrochemical potential were tuned in the same substrate in ionic liquid for the purpose of measuring the electronic state in SWNT. Figure 4.4 shows the polarized SERRS spectra with different half bandwidth. Figure 4.4 (a) has the 3.2 cm^{-1} and (b) has the 4.5 cm^{-1}. These difference comes from the $\sigma - \pi$ coupling of nanotube or doping density in the confined area on the SWNT[23]. Figure 4.5 show the polarized SERRS spectra under the electrochemical potential control. The RBM and G-band intensity are increased and decreased under the potential control. This tendency is suggested to be related to the depletion / filling of valence / conduction band. Figure 4.5 (a) shows intensity modulation without the band shift. Figure 4.5 (b) in the parallel polarization configuration shows the G-band intensity modulation with band shift. Figure 4.5 (c) shows the similar modulation in the G-band intensity and band shift in the perpendicular polarization configuration. The intensity and band shift profile as a function of the potential are shown in the figure 4.6. Calculated electronic density of state are shown in Figure 4.6 (a). The maximum Raman intensity was presented around the Fermi level. And the tendency of the Raman intensity presents the different tendency at $\pm E_1$, $\pm E_2$ levels. Frequency shift are increased around the $\pm E_2$ levels. In the more positive potential of $+E_1$ and $+E_2$ the resonant Raman intensity is attenuated because of the electron depletion of the valence band. More negative potential of $-E_1$ and $-E_2$ the resonant Raman intensity is also attenuated because of the electron filling of the conduction band.
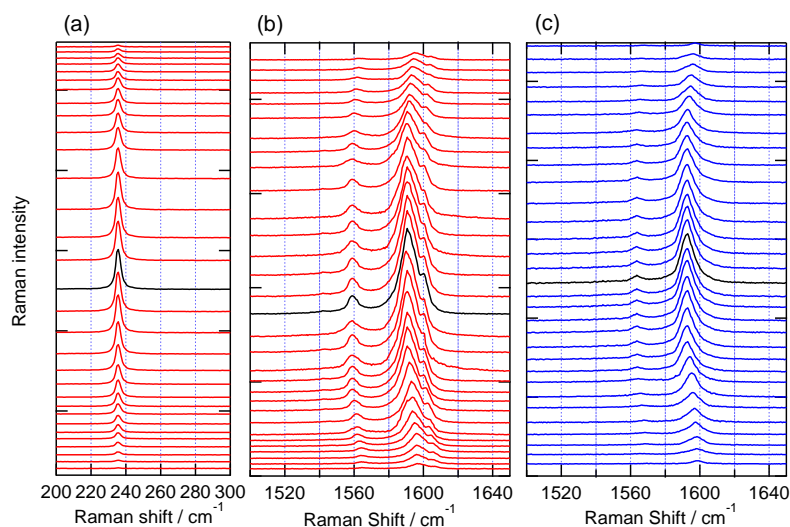
Figure 4.5 Polarized SERRS spectra under the electrochemical potential control of : parallel polarization configuration (a, b), perpendicular polarization configuration (c). RBM line width Γ_{RBM} = 4.5 cm^{-1}. The potential are +1.5 V to -1.5 V vs. Ag/Ag$^+$ from bottom to top in 0.1 V increment.
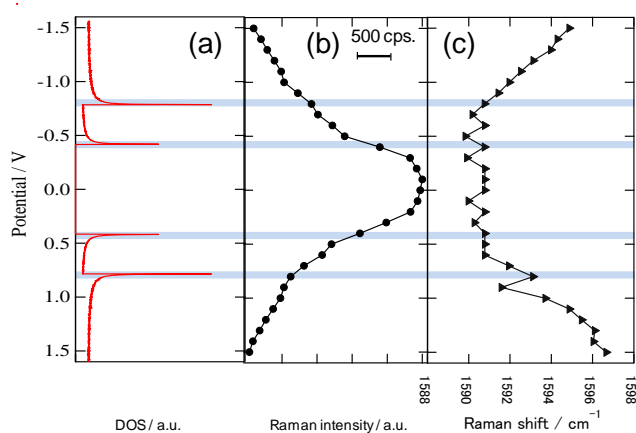

Figure 4.6 Raman intensity profile (b) and Raman frequency profile (c) and calculated electronic density of state (EDOS) of corresponding nanotube (a).

In the narrow RBM band width in Figure 4.4 (a), the fluctuations of the depolarization ratio were observed near the vHS (Figure 4.7). The electron filling of the valence band enhanced the E$_1$ mode at perpendicular polarization configuration. The E$_1$ mode are known to be E$_{n,n\pm1}$ transition in the

54

RRS spectrum. E_1 band intensity ratio are increased in the +0.9 V which is near to the $+E_2$ band. Additional transiton of $E_{2 \rightarrow 1}$ are suggested to enhance the perpendicular polarization signal.
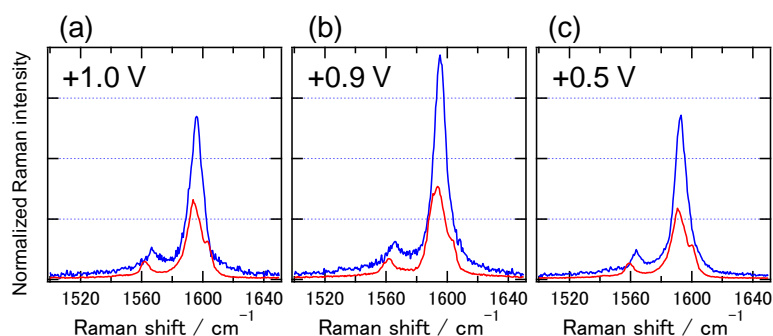

Figure 4.7 Polarized Raman spectra of normalized by the RBM band intensity at the each electrochemical potentials : +1.0 V (a), +0.9 V (b), +0.5 V (c). parallel polarization configuration (red line), perpendicular polarization configuration (blue line). Exposure time t_{ex} = 1 s and I_{ex} = 0.2 mW. Electrolyte were TMPA-TFSA, each potential versus Ag/Ag$^+$ TMPA-TFSA.

4.4 Conclusion

In this chapter I could obtain the isolated SWNT Raman spectra using the Au nanodimer arrays. The Au dimer structured on conductive substrate allowed to carry out for in-situ electrochemical Raman measurement. SERRS observed in the present system showed depolarized behavior especially in the specific G-band mode. G-band intensity especially in E_1 mode was enhanced at perpendicular polarization configuration near vHS. This tendency was proved that the additional transition on the vertical transition ($E_{2 \rightarrow 1}$) affected the perpendicular Raman signal enhancement. Electrochemical potential dependence suggests that highly localized anisotropic

electromagnetic field excites specific transition of $E_{2\to1}$ or $E_{1\to2}$, resulting in the formation of excited respective electrons and holes at more negative and positive potentials than those formed at normal light illumination in SWNT. Polarized surface-enhanced resonant Raman spectra clarified these characteristic transition of the electronic states under electrochemical potential control.

4.5 References

1.   Dresselhaus, M. S.; Dresselhaus, G.; Saito, R. *Phys. Rev. B* **1992,** 45, 6234-6242.

2.   Samsonidze, G. G.; Grüneis, A.; Saito, R.; Jorio, A.; Souza Filho, A. G.; Dresselhaus, G.; Dresselhaus, M. S. *Phys. Rev. B* **2004,** 69, 205402.

3.   Saito, R.; Fujita, M.; Dresselhaus, G.; Dresselhaus, M. S. *Appl. Phys. Lett.* **1992,** 60, 2204-2206.

4.   Samsonidze, G. G.; Saito, A. R.; Jorio, D. A.; Pimenta, E. M. A.; Souza Filho, E. A. G.; Grüneis, F. A.; Dresselhaus, D. G.; Dresselhausa, M. S. *J. Nanosci. Nanotechnol.* **2003,** 3, 431-458.

5.   Tans, S. J.; Devoret, M. H.; Dal, H.; Thess, A.; Smalley, R. E.; Geerligs, L. J.; Dekker, C. *Nature* **1997,** 386, 474-477.

6.   Samsonidze, G. G.; Saito, R.; Kobayashi, N.; Grüneis, A.; Jiang, J.; Jorio, A.; Chou, S. G.; Dresselhaus, G.; Dresselhaus, M. S. *Appl. Phys. Lett.* **2004,** 85, 5703-5705.

7.   Saito, R.; Dresselhaus, G.; Dresselhaus, M. S. *Phys. Rev. B* **2000,** 61, 2981-2990.

8.   Valentin, N. P. *New J. Phys.* **2004,** 6, 17.

9.   Telg, H.; Maultzsch, J.; Reich, S.; Hennrich, F.; Thomsen, C. *Phys. Rev. Lett.* **2004,** 93, 177401.

10.   Fantini, C.; Jorio, A.; Souza, M.; Strano, M. S.; Dresselhaus, M. S.; Pimenta, M. A. *Phys. Rev. Lett.* **2004,** 93, 147406.

11.   Popov, V. N.; Henrard, L.; Lambin, P. *Phys. Rev. B* **2005,** 72, 035436.

12.   Kataura, H.; Kumazawa, Y.; Maniwa, Y.; Umezu, I.; Suzuki, S.; Ohtsuka, Y.; Achiba, Y. *Synth. Met.* **1999,** 103, 2555-2558.

13.   Dresselhaus, M. S.; Dresselhaus, G.; Saito, R.; Jorio, A. *Phys. Rep.* **2005,** 409, 47-99.

14.   Jorio, A.; Souza Filho, A. G.; Dresselhaus, G.; Dresselhaus, M. S.; Swan, A. K.; Ünlü, M. S.; Goldberg, B. B.; Pimenta, M. A.; Hafner, J. H.; Lieber, C. M.; Saito, R. *Phys. Rev. B* **2002,** 65, 155412.

15.   Fantini, C.; Pimenta, M. A.; Strano, M. S. *J. Phys. Chem. C* **2008,** 112, 13150-13155.

16.   Jorio, A. *Phys. Rev. Lett.* **2003,** 90, 107403.

17.   Liu, C. y.; Bard, A. J.; Wudl, F.; Weitz, I.; Heath, J. R. *Electrochem. and Solid-State Lett.* **1999,** 2, 577-578.

18.   Heller, I.; Kong, J.; Heering, H. A.; Williams, K. A.; Lemay, S. G.; Dekker, C. *Nano Lett.* **2005,** 5, 137-142.

19.   Rao, A. M.; Eklund, P. C.; Bandow, S.; Thess, A.; Smalley, R. E. *Nature* **1997,** 388, 257-259.

20.   Kavan, L.; Rapta, P.; Dunsch, L. *Chem. Phys. Lett.* **2000,** 328, 363-368.

21.   Claye, A. S.; Nemes, N. M.; Jánossy, A.; Fischer, J. E. *Phys. Rev. B* **2000,** 62, R4845-R4848.

22.   Okazaki, K.-i.; Nakato, Y.; Murakoshi, K. *Phys. Rev. B* **2003,** 68, 035434.

23.   Murakoshi, K.; Okazaki, K.-i. *Electrochim. Acta* **2005,** 50, 3069-3075.

24.   Okazaki, K.-i.; Nakato, Y.; Murakoshi, K. *Surf. Sci.* **2004,** 566–568, 436-442.

25.   Heller, I.; Kong, J.; Williams, K. A.; Dekker, C.; Lemay, S. G. *J. Am. Chem. Soc.* **2006,** 128, 7353-7359.

26.   Frackowiak, E.; Béguin, F. *Carbon* **2001,** 39, 937-950.

27.   Frackowiak, E.; Béguin, F. *Carbon* **2002,** 40, 1775-1787.

28.   O'Connell, M. J.; Eibergen, E. E.; Doorn, S. K. *Nature Mat.* **2005,** 4, 412-418.

29.   Tanaka, Y.; Hirana, Y.; Niidome, Y.; Kato, K.; Saito, S.; Nakashima, N. *Angew. Chem. Int. Ed.* **2009,** 48, 7655-7659.

30.   Kalbac, M.; Farhat, H.; Kavan, L.; Kong, J.; Dresselhaus, M. S. *Nano Lett.* **2008,** 8, 3532-3537.

31.   Kalbac, M.; Hsieh, Y.-P.; Farhat, H.; Kavan, L.; Hofmann, M.; Kong, J.; Dresselhaus, M. S. *Nano Lett.* **2010,** 10, 4619-4626.

32.   Kalbac, M.; Farhat, H.; Kavan, L.; Kong, J.; Sasaki, K.-i.; Saito, R.; Dresselhaus, M. S. *ACS Nano* **2009,** 3, 2320-2328.

Chapter 5

Raman Enhancement via Polariton States Produced

by Strong Coupling between Localized Surface Plasmons

and Dye Excitons at Metal Nano-Dimer

5.1 Introduction

The character of the plasmon-induced photoexcitation process was modulated by the interaction between metal and molecules. The energy of photoexcitation process is limited by the intrinsic energy of the materials. The search for active interaction between metal and molecule is necessary to obtain the general versatility and wide-range use for photoexcitation. Intensive investigations of the interactions between the electronic states in organic molecules and plasmons have been undertaken. In particular, it was found that when an emitter situated near the metal surface interacts with the plasmon resonance, the spontaneous emission rate is modulated and the energy transfer rate is changed[1, 2]. Most studies, however, have been carried out in the weak coupling regime. On the other hand, pioneering studies proved that organic dye molecules with high oscillator strengths form strong coupling regimes under the excitation by plasmon[3-11]. The coupling strength can be controlled via the plasmon energy and its line widths. Furthermore, it has been found that hybrid states produced by strong coupling modulate the optical absorption and emission properties[3-5], the lifetimes of the excited states[6], and also the chemical reactivity[10] of the systems. Although many reports have observed strong coupling produced by surface plasmons[3, 6-9], application of the LSPR remains a challenging subject[12-16].

The photoexcitation characteristics of materials have been investigated using surface enhanced resonance Raman scattering (SERRS). Electronic excitation of molecules due to localized electromagnetic field leads to additional enhancement due to the optical absorption resonance at SERRS process. Previously documented studies have found that the absorption spectra of chromophores that were adsorbed to Au or Ag plasmonic nanoparticles can be strongly perturbed[17-22]. This perturbation of the electronic transition affects the SERRS profiles in ways that differ from those predicted based on simple enhancement of the local electromagnetic field[23-25]. Brus et al. described the SERRS effect as involving transition dipole coupling between the chromophore and the metal[26, 27]. Also, Mayer showed a theoretical simulation of the SERRS conditions that included resonance coupling between the molecular electronic transition and the optical transition of the nanoparticles[28]. Despite these attempts to research the Raman characteristics when the system achieved hybridized states[29], the Raman features in the strong coupling regime when using LSPR have not been clarified yet.

In this work, I report on the effects of Raman scattering on the formation of nanodimer–organic dye molecule complexes that achieve strong coupling between the plasmons of the nanodimer structure and the excitons of the adsorbed dye molecules.

5.2 Experimental

Ag dimer array were prepared by angle-resolved nanosphere lithography (AR-NSL) using repeated vapor depositions with different angles onto the PS particle (diameter $d = 350$ nm) monolayer prepared on a glass substrate. After the first deposition at $0°$ in the angle between the surface normal and the Ag deposition beam, the second deposition was carried out at the different angles, θ, varying from $19°$ to $23°$. The Ag-NSL substrate was obtained after removal of PS

particles (Figure 5.1 (a-d)).   The dye used is 1,1',3,3,3',3'-hexamethylindotricarbocyanine

perchlorate (HITC, CAS No. 16595-48-51, Figure 5.1 (e)).

HITC covered Ag-NSL substrate (Ag@HITC) was fabricated by dropping 100 μl of 10

μM HITC aqueous solution. After drying the HITC solution, extinction spectrum was acquired. For

Raman measurement, Ag-NSL substrate was rinsed in order to remove of residual HITC. Extinction

spectra of the metal dimer array in the visible-near infrared region were reorded utilizing a

multi-channnel spectrometer (MCPD-2000, Ohtsuka Electronics). The structure of the dimer on the

glass substrate was inspected by an atomic force microscope (AFM, Nanoscope-IIIa, Digital

Instruments) in air. A home-made polarized Raman microscope spectrometer was specially modified

for NIR laser light (r_{ex} = 785 nm, 1.58 eV)[chem. comm] with $100\times$ objective lens (Olympus, 1.0

NA). Raman measurements were carried out at the backscattering configuration collecting the

scattering photons with the parallel and perpendicular polarization directions simultaneously.
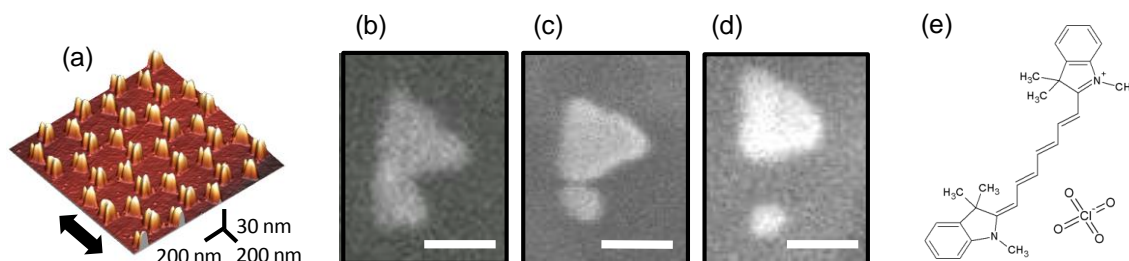

Figure 5.1. AFM image of the Ag-NSL substrate (d = 350 nm) (a); SEM image of the Ag-NSL

substrate (b-d), the second deposition angle θ = 19°(b), 21°(c), 23°(d), scale bar indicate 50 nm; the

HITC molecular structure (e).

5.3 Results and Discussion

The coupling strength is tuned using these nano-dimers with gap-mode plasmon wavelengths varying from 600 nm (2.07 eV) to 850 nm (1.46 eV) through the exciton energy of the organic dye molecule at 750 nm (1.65 eV). The plasmon energy was changed by varying the distance between the Ag dimers, which were prepared by angle-resolved nanosphere lithography (AR-NSL) on to a glass substrate (surface area = 1 cm^2)[30-33]. Estimated gap distance of tip-to-side triangular dimer structure with ca. 50 nm in side length and 30 nm in height is a few nm when the dimer structure shows extinction maximum at 785 nm (1.58 eV) for Raman excitation laser light polarized parallel to the long axis of the dimer structure (Figure 5.1 (a-d)). This gap distance was varied from zero to <18 nm for changing gap-mode plasmon wavelengths from 850 nm to 600 nm[30,]
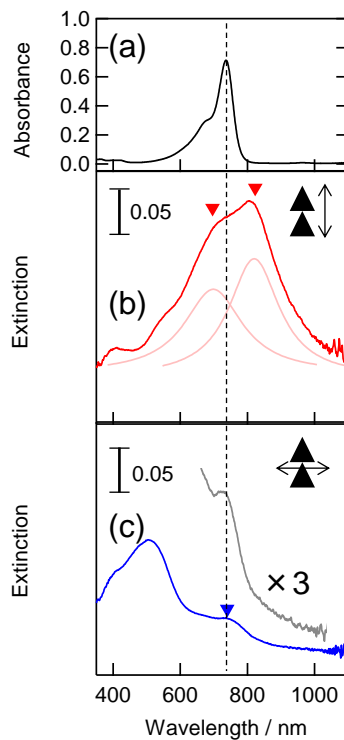

Figure 5.2. Absorption spectra of 10 mM HITC aqueous solution (a), extinction spectrum (b,c), incident polarization is parallel to the longer dimer axis(b) and shorter dimer axis(c).

[33, 34]. Polarized Raman measurements provide information about the contributions of the hybridized states at the metal dimer gap to the Raman enhancement. Figure 5.1(a) shows a typical atomic force microscopy (AFM) image of the Ag-NSL substrate. The directions of the long axis of the individual dimers were well aligned on the glass substrate. The dye used in the present system is 1,1',3,3,3',3'-hexamethylindotricarbocyanine perchlorate (HITC, Figure 5.1(e)). Figure 5.2 (a) shows the absroption spectrum of 10 mM HITC aqueous solution. The extinction spectrum was splitted into two bands at the incident light at parallel polarization along to dimer long axis as shown in Figure 5.2 (b). At the perpendicular polarization along to the dimer long axis extinction spectrum show the peak at dye exciton energy. For the evaluation of the splitted peak of extinction spectrum at
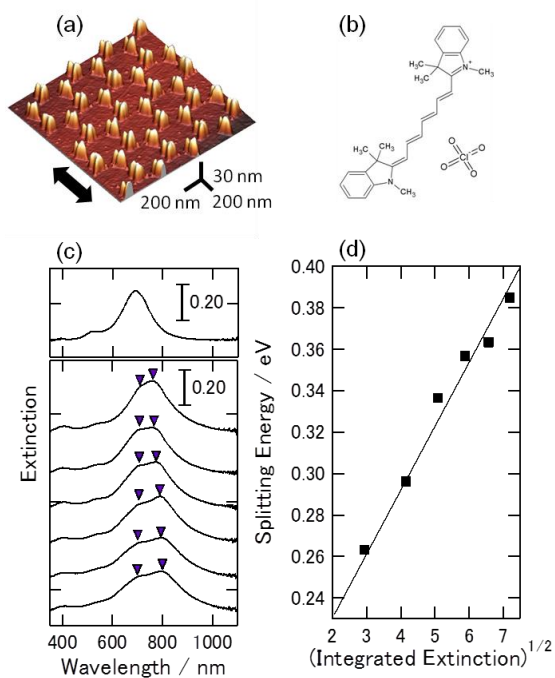

Figure 5.3. the polarized extinction spectrum of the bare Ag-NSL substrate, with the parallel polarization to the long axis of the dimers (a, upper column); the extinction spectrum of HITC deposited on Ag-NSL with increasing HITC coverage from top to bottom (a, bottom column); the corresponding energy of Rabi splitting as a function of the square root of the integrated extinction of the dye molecules (b).

paralle incident light, I checked the dependence on the amount of the dye layer. Figure 5.3 (a) show

a bare Ag-NSL substrate (top column), which shows a bare plasmon peak at 694 nm. The HITC

deposited on Ag-NSL substrate (Ag@HITC) was prepared by dropping 10 μM HITC aqueous

solution onto the Ag-NSL substrate. After drying of the HITC solution, extinction spectra were

acquired, and the resulting spectra are shown in the bottom column of Figure 5.3 (a). The spectral

change was observed as a split in the peak of the extinction. Peak wavelength can be estimated via

deconvolution of the observed spectrum into two distinct peaks. The separation of the peaks

increased as the amount of HITC used, as shown in Figure 5.3 (a), from top to bottom.

Figure 5.3 (b) shows the energy estimated from the peak separation as a function of a

square root of the integrated extinction of the glass substrate with the same amount of the dye

molecule as Ag@HITC. The splitting energy after the first deposition of 100 μl of a 10 μM HITC

aqueous solution was observed 0.26 eV. After repeated deposition for total 600 μl of a 10 μM HITC

aqueous solution, the splitting energy reached maximum value of 0.39 eV. Dependence of the values

of the splitting energy on the square root of the integrated extinction of the dye molecules shows

linear correlation as shown in Figure 5.3 (b). Observed energy splitting could be attributable to the

strong coupling between excitons in the dye molecules at the gap and localized plasmons of the

metal nanodimer. When plasmons and excitons achieve strong coupling, extinction spectrum shows

two extinction peaks with the energy separation characterized as

$$\Delta E_{Rabi} = \sqrt{\left(\hbar\Omega_R\right)^2 - \left(\gamma_{LSP} - \gamma_{HITC}\right)^2} \text{ ,} \qquad (5.1)$$

where ΔE_{Rabi} is the Energy separation between extinction peaks; $\hbar\Omega_R$ is the coupling energy

due to Rabi splitting; γ_{LSP} and γ_{HITC} are LSP resonance and molecular resonance linewidths[16]. The

observed splitting energy of 0.39 eV may reflect the coupling of the LSPR and the excitons of the

HITC molecules. In the theoretical calculation, the Rabi splitting occurs when

$\hbar\Omega_R < (\gamma_{LSP} - \gamma_{HITC})/2$ [34]. Based on the values of the relative resonance linewidths ($\gamma_{LSPR} = 0.14$ eV and $\gamma_{HITC} = 0.05$ eV), the observed splitting energy agrees with the values of the strong coupling regime in previously documented results[16] and theoretical studies[34]. Although the value of the mode volume of the LSPR field produced by the metal nanodimer structure used here is difficult to define, localization of the photon field of the present system less than a few nm^3 in space suggests the contribution of a relatively small number of molecules at the gap to the strong coupling regime[35,36]. In the strong coupling regime, the coupling energy has the correlation

$$\hbar\Omega_R \propto f'^{\frac{1}{2}} \qquad (5.2)$$

where f' is effective oscillator strength, as $f' = nf$. n is the number of oscillator in the photon field and f is the oscillator strength of a single molecule. Thus, observed splitting energy is linearly correlated to the square root of integrated extinction of the system in strong coupling regime. This relation have been observed at the system of organic molecules in subwavelength hole arrays[7] and dyes in micro-cavities[4, 37, 38]. In the present system, the effective oscillator strength should increases as the number of molecules in the gap increases by repeated depositions of the dye solution. Observed linear relation in Figure 5.3(b) reflects increment of the number of dye molecules whose direction of the induced dipole matches to that of localized electromagnetic field at the gap. The observed maximum splitting energy achieved up to 0.39 eV, which is comparable to the largest values that have been reported to date[14-16, 29]. In the present system, monomer HITC molecules may contribute to the strong coupling, because the localized plasmons (730 nm, 1.70 eV) are energetically matched to the monomer absorption band (736 nm, 1.68 eV), because the H-aggregated molecules exhibit a blue-shifted absorption band (678 nm, 1.83 eV)[15].

Figure 5.4 (a) shows the extinction spectra of the bare Ag-NSL substrates with distinct gap distances of the Ag nano-dimer. The LSPR wavelength can be varied from 600 nm (2.07 eV) to 850

nm (1.46 eV), depending on the dimer gap distance[30]. After the substrates deposted HITC, the bare

plasmon peak split into two peaks, as shown in Figure 2(b). Substrate-dependent energy splits shown

in Figure 5.4 (b) reflect the difference in the coupling strength between the dye excitons and the

localized plasmons with distinct energy at respective Ag-NSL substrates. The extinction under the

perpendicular polarization to the long dimer axis of the metal nanostructure (dotted lines in Figure

5.4 (a)) shows negligibly small extinction at the wavelength region of the plasmon band observed at

the parallel polarization (solid lines in the same Figure 5.4 (a)), indicating that the contribution of the

extinction due to the monomer and aggregates which do not have significant coupling with the

localized plasmons is quite small (less than 2×10^{-2}). The amounts of the dye deposited on the

substrates are fixed by adjusting the amount of the dye solution at the deposition to be the same

(total 600 μl). I optimized the amount of the dye on the substrate resulting in the maximum energy of

Rabi splitting, not to be deposited excess dye molecules which do not contribute the strong coupling.

Thus, respective substrates with distinct splitting energies are expected be under the condition with

comparable amounts of the dye at gap. Observed substrate dependence proves that only the excitons

in the dye molecules at the gap of the metal nanostructure contribute to the apparent change in the

extinction spectra shown in Figure 5.4 (a) to 5.4 (b), even though number of molecules at the gap is

much smaller than the total number of the dye molecules on the substrate.

These Ag@HITS substrates show distinct Raman intensities (Figure 5.4 (c)). The

maximum enhancement occurred at the substrate with the maximum absorption of the polariton at

the Raman excitation wavelength of 785 nm (1.58 eV) (5th from the top in Figure 5.4 (c)). The

dependence of the Raman intensity on the substrate clearly indicates that the new hybridized states

that were formed via strong coupling can contribute to the enhancement of the Raman scattering

process. It should be noteworthy that the substrates showed highly polarized Raman scattering

characteristics. Apparent scattering was only observed at parallel scattering configuration under the

excitation parallel to the long axis of the dimer (solid lines in Figure 5.4 (c)). Raman scattering was not observed at the perpendicular scattering configuration under parallel excitation (dotted lines in Figure 5.4 (c)). Observed characteristics of polarized Raman measurement prove that dye molecules at the gap of the dimer contribute to the Raman scattering process. Considering the fact that the amounts of dye molecules at the gap were comparable at respective substrates, variation of the Raman scattering intensity observed in the present systems could reflect difference in the resonance Raman process via the new hybridized states produced by the strong coupling of the excitons with localized plasmons.

Although the intensities are dependent upon the coupling strength, the Raman spectra are not significantly changed by the strength. The peaks of the Raman spectra at 133 and 298 cm^{-1} are assigned to the molecule's structural vibrations, and those at 501, 554, 797, 929 and 1126 cm^{-1} are assigned to the C-C stretching mode[39]. Although the Raman frequencies of these vibrational modes observed at crystalline HITC and Ag@HITC are the same, the SERS spectra of Ag@HITC show different relative intensity of these vibrational modes compared with those in the Raman spectra of crystalline HITC[39]. The C-C stretching modes of the SERS spectra become weaker than those of the Raman spectrum of crystalline HITC. These intensity ratios of the Raman spectra of the strong coupling system reflect the orientations of molecules in the highly localized anisotropic electromagnetic fields at the gap of the dimer.

Figure 5.5 (a) depicts the energy of the polariton peak against the energy of the plasmon peak observed at the bare Ag-NSL substrates. The diagonal solid line and the transverse dashed line indicate the plasmon and exciton positions, respectively. The plot shows anti-crossing behavior, also indicating that the present system can undergo strong coupling with LSPR and the dye excitons as
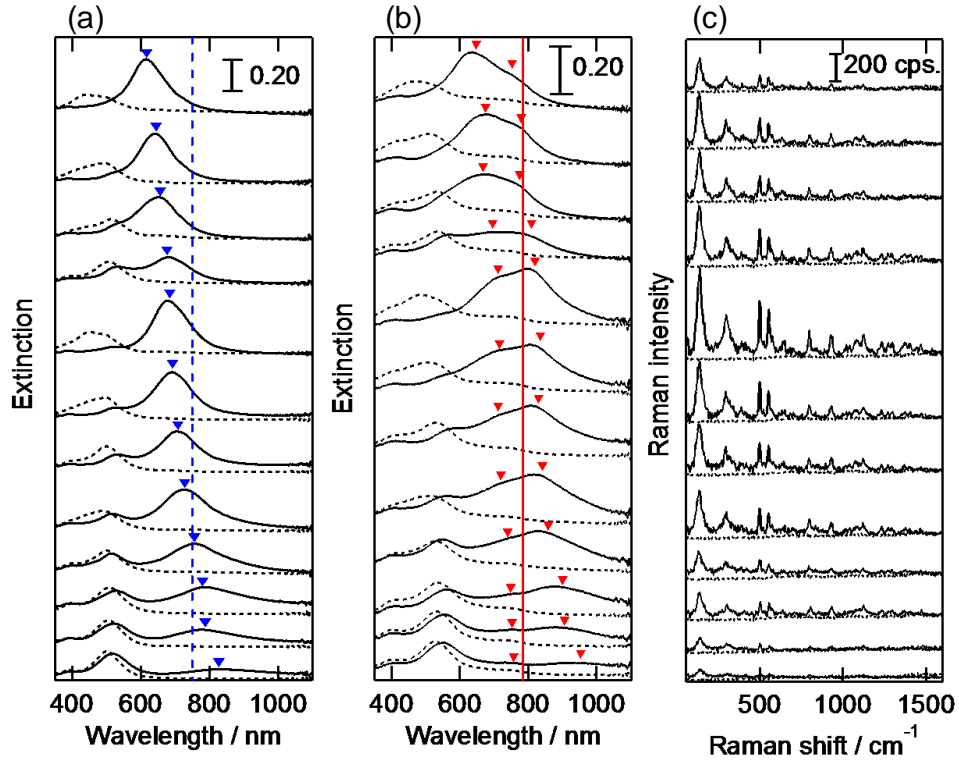
Figure 5.4. Polarized extinction spectra from the bare Ag-NSL substrates with distinct gap distance [where the polarization angles of incident light to the long axis of the dimers were parallel (solid line) and perpendicular (dotted line)], and the HITC extinction peak [736 nm (1.68 eV, blue broken line)] (a); the corresponding polarized extinction spectra of Ag@HITC, and the Raman excitation energy [785 nm (1.58 eV, red solid line)] (b); corresponding polarized Raman spectra observed in the Ag@HITC [scattering parallel (solid line) and perpendicular (dashed line) with extinction parallel to the dimer axis] (where I_{ex} = 50 μW, and t_{sec} = 1 s) (c).

proved by the linear dependence of the variation of the Rabi splitting as a function of the square root of the integrated extinction (Figure 5.3 (b)). When these polariton energies are compared with the energy of the Raman excitation (785 nm, 1.58 eV) shown in Figure 5.5 (a) as a red line, the energy of the lower branches of the polariton matches that of the Raman excitation in the present

67

system, especially at the substrate with the plasmon peak at 1.8 eV.   This substrate shows the most intense Raman scattering from molecules in the strong coupling regime as shown in the spectrum (5th from the top in Figure 5.4).   The excitation laser wavelength corresponds to lower energy polariton of the substrate shown at the tops of Figure 5.4 (b), and to higher energy polariton at the bottoms of Figure 5.4 (b).

To estimate the effect of the excitation of the upper and the lower branches of the polariton, observed Raman intensity is compared with the extinction intensity of the polariton. Figure 5.5 (b) shows the Raman intensity in the 133 cm^{-1} band against the corresponding extinction intensity at Ag@HITC. The Raman intensity increases linearly with the increasing the extinction of the polariton. This linear relationship suggests that strong enhancement of the Raman process can occur when a polariton excitation lies within the Raman excitation (1.58 eV (785 nm)) and scattering processes (133 cm^{-1} Raman shifted photons at 1.56 eV (793 nm)). A strong Raman signal originates
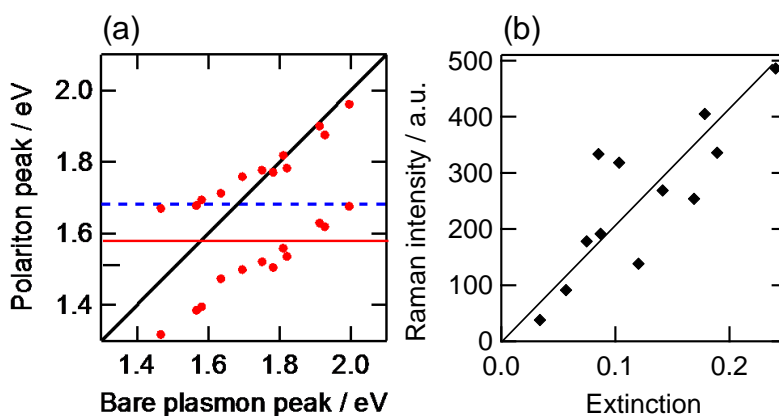

Figure 5.5. Positions of the peaks in Figure 2(b) plotted against the corresponding bare LSPR positions (red circles), where the blue dashed line represents the uncoupled HITC exciton energy [1.68 eV (736 nm)], and the red solid lines represent the Raman excitation energy [1.58 eV (785 nm)] (a); Raman intensity of 133 cm^{-1} band plotted against the corresponding extinction of Ag@HITC.

from the resonance with the upper as well as the lower branches of the polariton. In the case of cavity Raman enhancement in a semiconductor quantum well, the polariton in the lower branch shows higher enhancement than that in the upper branch[40]. The slower dephasing of the polaritons in the lower branch has been considered to result in higher Raman enhancement. In the strong coupling regime between the dye exciton and LSP, photoluminescent is only observed from the lower polariton branch, because the dephasing rate of the polariton in the higher polariton branch is faster than that in the lower polariton branch[6].   Further quantitative measurement using the system with controlled number of molecules at the nanogap could clarify the difference in the effect of the excitation to the upper and the lower branches of the polariton on the Raman scattering from molecules under strong coupling conditions at LSP. Raman scattering intensity also may reflect the effects of the coupling of the light in and out with plasmonic metal nanostructure. Purcell effect could be one of the possibilities to change the scattering efficiency of confined light far below the diffraction limit. At the present, the contribution of Purcell effect has not clarified yet, compared with previously documented results shown in SERS[43] and other fluorescence enhancement experiments[42].

5.4 Conclusion

In conclusions, I prepared a system that shows strong coupling between the LSPR and dye excitons using Ag dimer structures and HITC molecules. Despite the broad absorption band of HITC, a relatively large Rabi splitting energy can be achieved by tuning the LSPR energy through careful control of the metal nano-gap distance. Polarized Raman measurement proves the contribution of the strong coupling at the nanogap to Raman enhancement, indicating that well-defined interactions occur between the molecule electronic states and the confined electromagnetic field. The maximum Raman enhancement was obtained at the resonant energy between the hybrid states and the excitation. The Raman enhancement in the strong coupling regime allows us to observe the vibrational structure in the new hybridized molecule states for the first time. This will guide us toward detailed understanding of the excitation process the selectively polarized excitation of molecules in the confined nano-size electromagnetic fields. The system described here offers interesting possibilities for use of the strong interaction between the molecules and the localized plasmons, and may possibly be applied to the development of a novel photochemical reaction using LSPs.

5.5 References

1.   Drexhage, K. H., IV Interaction of Light with Monomolecular Dye Layers. In *Progress in Optics*, Wolf, E., Ed. Elsevier: 1974; Vol. Volume 12, pp 163-232.

2.   Pettinger, B. *J. Chem. Phys.* **1986,** 85, 7442-7451.

3.   Pockrand, I.; Brillante, A.; Mobius, D. *J. Chem. Phys.* **1982,** 77, 6289-6295.

4.   Lidzey, D. G.; Bradley, D. D. C.; Skolnick, M. S.; Virgili, T.; Walker, S.; Whittaker, D. M. *Nature* **1998,** 395, 53-55.

5.   Lidzey, D. G. *Science* **2000,** 288, 1620-1623.

6.   Bellessa, J.; Bonnand, C.; Plenet, J.; Mugnier, J. *Phys. Rev. Lett.* **2004,** 93, 036404.

7.   Dintinger, J.; Klein, S.; Bustos, F.; Barnes, W.; Ebbesen, T. *Phys. Rev. B* **2005,** 71, 035424.

8.   Sugawara, Y.; Kelf, T. A.; Baumberg, J. J.; Abdelsalam, M. E.; Bartlett, P. N. *Phys. Rev. Lett.* **2006,** 97, 266808.

9.   Hakala, T.; Toppari, J.; Kuzyk, A.; Pettersson, M.; Tikkanen, H.; Kunttu, H.; Törmä, P. *Phys. Rev. Lett.* **2009,** 103, 053602.

10.   Hutchison, J. A.; Schwartz, T.; Genet, C.; Devaux, E.; Ebbesen, T. W. *Angew. Chem. Int. Ed.* **2012,** 51, 1592-1596.

11.   Hutchison, J. A.; Liscio, A.; Schwartz, T.; Canaguier-Durand, A.; Genet, C.; Palermo, V.; Samori, P.; Ebbesen, T. W. *Adv. Mater.* **2013,** 25, 2481-2485.

12.   Wiederrecht, G. P.; Wurtz, G. A.; Hranisavljevic, J. *Nano Lett.* **2004,** 4, 2121-2125.

13.   Wurtz, G. A.; Evans, P. R.; Hendren, W.; Atkinson, R.; Dickson, W.; Pollard, R. J.; Zayats, A. V.; Harrison, W.; Bower, C. *Nano Lett.* **2007,** 7, 1297-1303.

14.   Fofang, N. T.; Park, T. H.; Neumann, O.; Mirin, N. A.; Nordlander, P.; Halas, N. J. *Nano Lett.* **2008,** 8, 3481-3487.

15.   Ni, W.; Ambjornsson, T.; Apell, S. P.; Chen, H.; Wang, J. *Nano Lett.* **2010,** 10, 77-84.

16.   Schlather, A. E.; Large, N.; Urban, A. S.; Nordlander, P.; Halas, N. J. *Nano Lett.* **2013,** 13, 3281-3286.

17.   Ru Lu, E. C.; Etchegoin, P. G., *Principles of Surface-Enhanced Raman Spectroscopy: and related plasmonic effects*. Elsevier Science: 2008.

18.   Makarova, O. V.; Ostafin, A. E.; Miyoshi, H.; Norris, J. R.; Meisel, D. *J. Phys. Chem. B* **1999,** 103, 9080-9084.

19.   Kometani, N.; Tsubonishi, M.; Fujita, T.; Asami, K.; Yonezawa, Y. *Langmuir* **2001,** 17, 578-580.

20.   Franzen, S.; Folmer, J. C. W.; Glomm, W. R.; O'Neal, R. *J. Phys. Chem. A* **2002,** 106,

6533-6540.

21.   Ipe, B. I.; Thomas, K. G. *J. Phys. Chem. B* **2004,** 108, 13265-13272.

22.   Lim, I. I. S.; Goroleski, F.; Mott, D.; Kariuki, N.; Ip, W.; Luo, J.; Zhong, C. J. *J. Phys. Chem. B* **2006,** 110, 6673-6682.

23.   Moskovits, M. *J. Raman Spectrosc.* **2005,** 36, 485-496.

24.   Weitz, D. A.; Garoff, S.; Gersten, J. I.; Nitzan, A. *J. Chem. Phys.* **1983,** 78, 5324-5338.

25.   Yang, W. H.; Schatz, G. C.; Vanduyne, R. P. *J. Chem. Phys.* **1995,** 103, 869-875.

26.   Jiang, J.; Bosnick, K.; Maillard, M.; Brus, L. *J. Phys. Chem. B* **2003,** 107, 9964-9972.

27.   Michaels, A. M.; Jiang, J.; Brus, L. *J. Phys. Chem. B* **2000,** 104, 11965-11971.

28.   Kelley, A. M. *J. Chem. Phys.* **2008,** 128, 224702.

29.   Cade, N.; Ritman-Meer, T.; Richards, D. *Phys. Rev. B* **2009,** 79, 241404.

30.   Sawai, Y.; Takimoto, B.; Nabika, H.; Ajito, K.; Murakoshi, K. *J. Am. Chem. Soc.* **2007,** 129, 1658-1662.

31.   Takase, M.; Sawai, Y.; Nabika, H.; Murakoshi, K. *J. Photochem. Photobiol. A* **2011,** 221, 169-174.

32.   Takase, M.; Nabika, H.; Hoshina, S.; Nara, M.; Komeda, K.; Shito, R.; Yasuda, S.; Murakoshi, K. *Phys. Chem. Chem. Phys.* **2013,** 15, 4270 – 4274.

33.   Sawai, Y.; Takimoto, B.; Nabika, H.; Ajito, K.; Murakoshi, K. *Faraday Discuss.* **2006,** 132, 179-190.

34.   Savasta, S.; Saija, R.; Ridolfo, A.; Di Stefano, O.; Denti, P.; Borghese, F. *ACS Nano* **2010,** 4, 6369-6376.

35.   Takase, M.; Ajiki, H.; Mizumoto, Y.; Komeda, K.; Nara, M.; Nabika, H.; Yasuda, S.; Ishihara, H.; Murakoshi, K. *Nature Photon.* **2013,** 7, 550-554.

36.   Aikens, C. M.; Madison, L. R.; Schatz, G. C. *Nature Photon.* **2013,** 7, 508-510.

37.   Hobson, P. A.; Barnes, W. L.; Lidzey, D. G.; Gehring, G. A.; Whittaker, D. M.; Skolnick, M. S.; Walker, S. *Appl. Phys. Lett.* **2002,** 81, 3519.

38.   Skolnick, M. S.; Fisher, T. A.; Whittaker, D. M. *Semicond. Sci. Technol.* **1998,** 13, 645.

39.   Akins, D. L.; Özçelik, S.; Zhu, H.-R.; Guo, C. *J. Phys. Chem. A* **1997,** 101, 3251-3259.

40.   Fainstein, A.; Jusserand, B., Raman Scattering in Resonant Cavities. In *Light Scattering in Solid IX*, Cardona, M.; Merlin, R., Eds. Springer Berlin Heidelberg: 2007; Vol. 108, pp 17-110.

41.   Yoshida, K.-i.; Itoh, T.; Tamaru, H.; Biju, V.; Ishikawa, M.; Ozaki, Y. *Phys. Rev. B* **2010,** 81, 115406.

42.   Yuan, H.; Khatua, S.; Zijlstra, P.; Yorulmaz, M.; Orrit, M. *Angew. Chem. Int. Ed.* **2013,** 52, 1217-1221.

Chapter 6

Electrochemical Control of Strong Coupling between

Localized Surface Plasmons and Dye Excitons

6.1 Introduction

It has been realized that localized surface plasmon (LSP) resonance can be strongly coupled to the excited states of molecules situated on the nano-sized metal surface in Chapter 5. Localized surface plasmon can be regarded as confined light to provide, highly polarized electromagnetic field with the specific resonant energy which can interact to excitons of materials effectively[1-9]. Thus, especially in the strong coupling regime by using LSP these properties attract the wide research interest as an entirely new concept of molecular-plasmonics. The excited state is considered to new energy state which is not limited by inherent energy state of materials. The concept will extend the plasmon-induced photo-excitation processes. If we can control of the state in strong coupling regime, it would be one of the approaches for tuning the photo-excited state. In the propagating plasmon resonance such as flat metal surface[10, 11], nano-hole array[12], and nano-grating[13, 14], it was reported that the strong coupling state provided the modulation of the lifetime of the excited states and of the absorption and emission properties[15-17]. The modulated property was reflected to the non-linear reactivity of the chemical reaction[18] and tuning the work function[19] via strong coupling and thermodynamics[20]. The use of propagating surface plasmon resonance is easily able to evaluate either the system is achieved to strong coupling regime or not. The energy dispersion was evaluated by changing the angle of the incident light, which cause the wavevector

change about the same environment of the substrate. In addition, the photoisomerization of dye molecules can tune the effective oscillator strength by just light illuminating or heating the substrate[21, 22] and gas flowing[23]. In contrast to the propagating surface plasmon resonance, the energy of the localized surface plasmon resonance was defined individually by the shape and size of the nano-structure. Distribution of the plasmon energy leads to the difference in the state of the strong coupling. At the present, control in the coupling of the system can be only achieved by the tuning the properties of dye molecules.

It is known that the resonant energy of LSPR can control by tuning electronic property in the electrochemical environment. In the metal nanoparticle system, it is found that the localized surface plasmon band moves lower (or higher) as the core is electrolytically made more electron deficient (or electron excess)[24, 25]. Electrochemical potential tuning in the strong coupling regime is able to characterize the LSP energy which concerns the dispersion about the coupling. In this chapter electrochemical potential control is adopted for tuning the LSPR energy and definition of the electronic properties of the strong coupling regime. Raman spectra also acquired for exploring the molecular state in strong coupling regime.

6.2 Experimental

Au nanostructure (Au-NSL) was prepared by using the angle-resolved nano-phere lithography technique. For electrochemical measurement the PS beads (diameter $\phi = 350$ nm) monolayer on indium tin oxide (ITO) glass were prepared. Au monomer structure were prepared after single deposition whose angle was vertical on the glass and thickness was 20, 30, 40 nm. Then PS mask was removed by sonication in Milli-Q water. The dye used is 1,1',3,3,3',3'- hexa methylindotricarbocyanine perchlorate (HITC). After dye deposition (600 μL / cm^{-1}), residual dye

molecules were rinsed by Milli-Q water. Dye coated Au monomer on ITO glass and bare Au monomer on ITO glass were used as working electrode. The Pt plate was used as counter electrode. The potential of the working electrode was regulated with respect to the Ag/AgCl reference electrode.

In electrochemical environment, the extinction spectrum and the Raman spectrum were acquired in-situ. The three electrode electrochemical cell was designed. Extinction spectrum of the Ag dimer array in the visible-near-infrared region was recorded utilizing a multichannel spectrometer (MCPD-2000, Ohtsuka Electronics, observed area was ~0.3 cm^2).

In the electrochemical environment, Raman measurement was performed in the backscattering configuration. Objective lens ($\times$100) which immersed in the water was used for in-situ Raman measurement. Excitation energy was λ_{ex} = 785 nm and exposure time was t = 1 s. The expanded NIR beam is focused onto the sample using a water-immersion objective lens with $\times$100 magnification and a numerical aperture of 1.0. The estimated spot size of irradiation ca. 1 μm, with output intensity was in 50 μW. All of Raman measurement was carried out in-situ by immersion of the Au-NSL substrate into aqueous solution containing 0.1 M NaClO$_4$ as electrolyte.

The structure of the Au monomer on the ITO glass substrate was inspected by an atomic force microscope (AFM, Nanoscope-IIIa, Digital Instruments) in air and scanning electron microscope (SEM, JSM-6700FT, JEOL).

6.3 Results and Discussion

The Au-NSL structures on ITO glass substrate were shown in Figure 6.1. Nanostructures were prepared by changing the Au deposition thickness (20, 30, 40 nm) on the ITO glass. Figure 6.1 (a, d, g) show the 20 nm (Au20), Figure 6.2 (b, e, h) were deposition of 30 nm (Au30) and Figure 6.1

(c, f, i) show the deposition of 40 nm (Au40). Triangle monomers were observed from SEM image (Figure 6.1 top and middle) and the height were confirmed from AFM image (Figure 6.1 bottom). The length of the perpendicular bisectors of the equilateral Au triangles was approximately 90 nm.

The extinction spectra of Au-NSL immersed in 0.1 M $NaClO_4$ aqueous solution were exhibited in the Figure 6.2 (a). These structures showed the peaks around the 800 nm and the peak energy was shifted on depending on the thickness of Au. The maximum peak wavelength was plotted against the Au nanoparticle's height as shown in Figure 6.2 (b). Higher nanoparticle shows the blue shifted peak of LSP. The observed peak in 0.1 M $NaClO_4$ aqueous solution was blue-shifted from compared with that in air. The peak shift occurs because of the change in dielectric environments in air ($n = 1.00$) and in 0.1 M $NaClO_4$ aqueous solution ($n = 1.33$)[26].
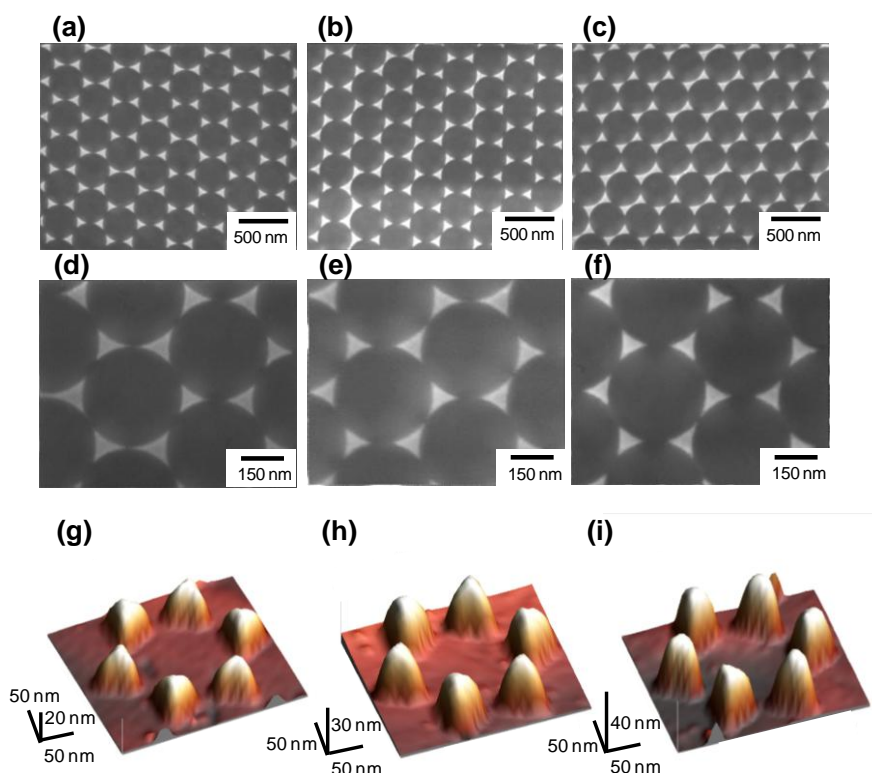
Figure 6.1 SEM (a - f) and AFM (g - i) image of Au-NSL: Au thickness 20 nm (a, d, g : Au20), 30 nm (b, e, h : Au30), 40 nm (c, f, i : Au40).
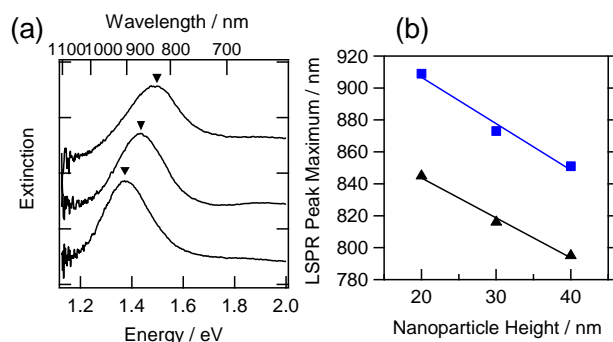
Figure 6.2 Extinction spectra of Au-NSL (a) and LSP peak maximum shift against the nanoparticle height (b): Au height 20 nm (a, top), 30 nm (a, middle), 40 nm (a, bottom), the LSPR peak in air (b, square), in 0.1 M NaClO$_4$ aqueous solution (b, triangle).

Figure 6.3 shows the extinction spectrum under electrochemical potential control of the Au-NSL substrate deposited HITC (top : Au@HITC) and the bare Au-NSL substrate (bottom). After deposition of the HITC, the observed peaks at +0.3 V were 1.48 eV (839 nm) in Au20@HITC (Figure 6.3 (a)) and the peak was shifted to 1.58 eV (787 nm) at -0.9 V. In Au30@HITC (Figure 6.3 (b)) the peak at +0.3 V were 1.69 eV (735 nm) and 1.50 eV (826 nm), and blue shifted to 1.76 eV (705 nm) and 1.65 eV (752 nm) at -0.9 V. In Au40@HITC (Figure 6.3(c)) the peak at +0.3 V were 1.79 eV (693 nm) blue shifted to 1.79 eV (692 nm) at -0.9 V and 1.64 eV (758 nm) at +0.3 V was decreased of the intensity.

And the bare Au substrate, the observed peaks of Au20 were 1.36 eV (909 nm) at +0.3 V and 1.45 eV (855 nm) at -0.9 V (Figure 6.3 d), the observed peaks of Au30 were 1.42 eV (873 nm) at +0.3 V and 1.52 eV (814 nm) at -0.9 V (Figure 6.3 e), the observed peaks of Au40 were 1.46 eV (851 nm) at +0.3 V and 1.55 eV (802 nm) at -0.9 V (Figure 6.3 f). The behavior of blue shift of the LSPR energy at positive polarization was reported previously[24, 25]. In the bulk metal, the real part of the dielectric function can be expressed approximately as

$$\varepsilon_c{}' = \varepsilon^{\infty} - \frac{\lambda_{peak}^2}{\lambda_p^2} \quad (6.1)$$

where λ_p is the bulk metal plasmon wavelength. λ_p is given by

$$\lambda_p = \frac{2\pi c}{\omega_p} \qquad (6.2)$$

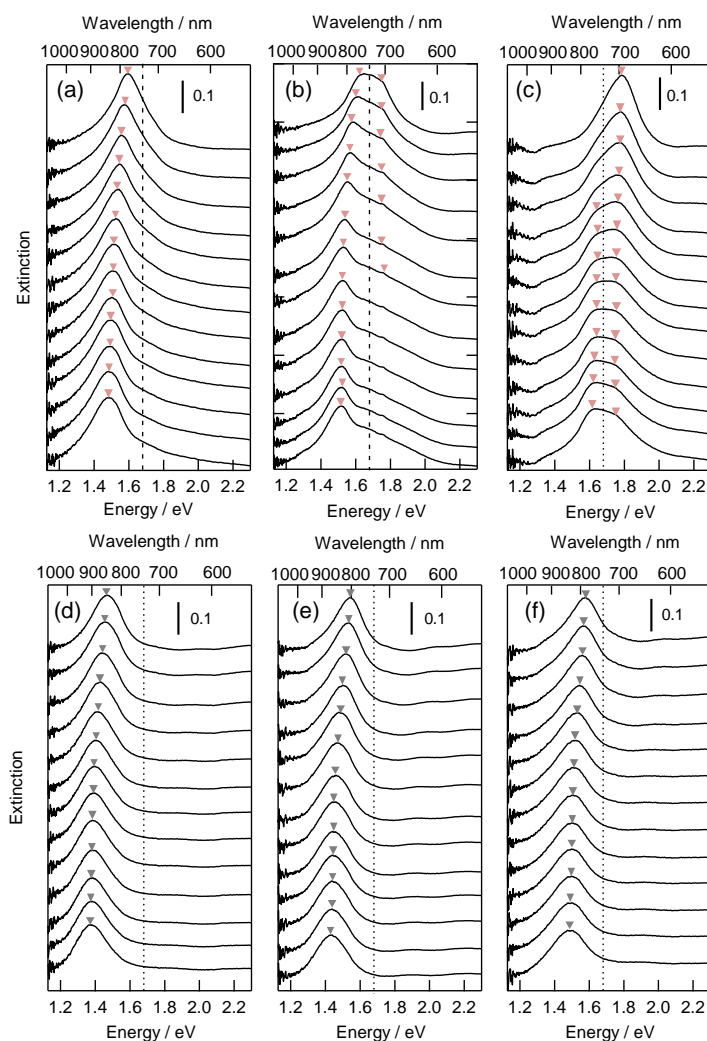where c is the speed of light in vacuum, ω_p is the metal's bulk frequency. ω_p is given by

Figure 6.3 extinction spectra in 0.1 M NaClO$_4$ aqueous solution : Au20@HITC (a), Au30@HITC (b), Au40@HITC (c), Au20 (d), Au30 (e), Au40 (f), dotted line was exciton energy of HITC. The electrochemical potential were from +0.3 V of bottom to -0.9 V of top, spectra were acquired in each 0.1 V change.

$$\omega_p = \left(\frac{Ne^2}{m\varepsilon_0} \right)^{1/2} \quad (6.3)$$

where N is the free electron concentration, m is the electron mass. In electrochemical condition,

N can be varied by changing electrochemical potential of metals, leading to the change in ω_p.

Relation between the free electron concentration and the SP band wavelength derived from

equations (6.1), (6.2) and (6.3), to give

$$\left[\frac{\lambda_{peak}^{final}}{\lambda_{peak}^{init}} \right] = \left[\frac{N_{init}}{N_{final}} \right]^{\frac{1}{2}} \quad (6.4)$$

where $\lambda_{peak}^{init}, \lambda_{peak}^{final}$ is the peak wavelength in initial and final state, and N_{init}, N_{final} is the free

electron concentration. This relation can be applied to LSPR at metal nanoparticle. In the present

system, negative polarization from +0.3 V to -0.9 V resulted in the blue shift of λ_{peak} by 54 nm for

Au20, reflecting estimated decrease in N for 3.1 %. At Au30 and Au40, the shift of 59 nm and 49
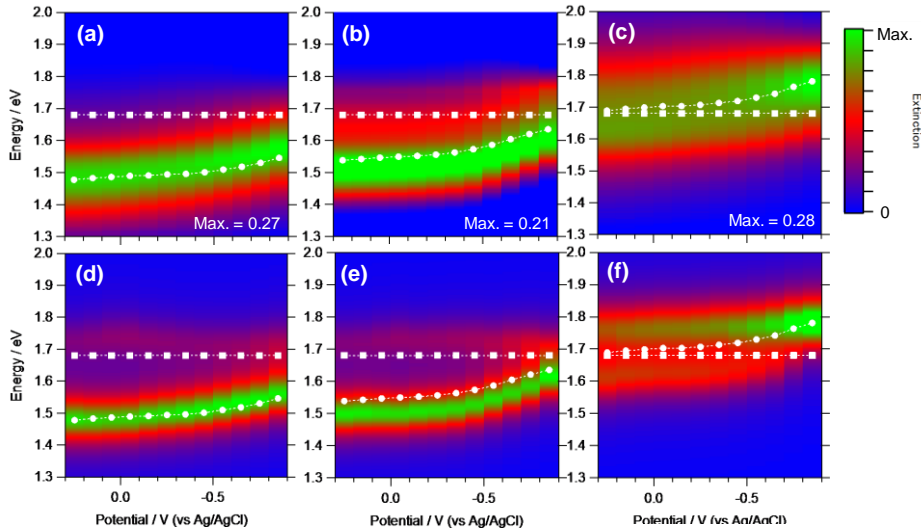

Figure 6.4 Image plot of the extinction spectra against the electrochemical potential : Au20@HITC

(a), Au30@HITC (b), Au40@HITC (c), the exciton energy of HITC (1.68 eV, circle) and the

estimated LSPR band energy (square) were plotted against the electrochemical potential.

nm correspond to estimated decrease in N for 3.5 % and 3.0 %, respectively. Comparable change

in λ_{peak} was reported previously at the system of Au nanoparticles on Pt mesh substrate in 0.1 M

Bu$_4$NPF$_6$/CH$_2$Cl$_2$. Positive polarization for about 1.0 V from -0.16 V to +0.82 V vs Ag/Ag$^+$ resulted

in the shift of λ_{peak} for 9 nm from 525 nm to 516 nm, corresponding to the decrese in N for 5 %.

Based on these observations at the present system, I could estimate possible shift of λ_{peak}

depending on the electrochemical potential of the system at the strong couple regime. I assumed that

the peak shift of λ_{peak} at the dye deposited substrate should be comparable those without dye,

because the thickness is same.

In -0.9 V at Au30@HITC (Figure 6.3 (b)), center of peak energy go over the energy of

HITC exciton. When the dye exciton energy and plasmon energy were same, the strong coupling

was achieved and in addition the energy separation is the same from the exciton energy. Then, the

plasmon mode at -0.9 V was estimated in the same energy of HITC exciton (1.68 eV). In +0.3 V of

Au30@HITC LSPR position were estimated from the ratio of the free electron concentration of

Au30 by using equation (6.4). Figure 6.4 show the image plot of the extinction spectra of Au@HITC

at each Au monomer height. The estimated LSP position (Figure 6.4, white circle) and exciton

energy position of HITC (Figure 6.4, white square) were plotted against the electrochemical

potential. As shown in figure 6.4 (c) at +0.3 V the LSPR and HITC energy were coincident and the

strong coupling regime was achieved and then at -0.9 V the LSPR were apart from the HITC exciton

energy. Thus electrochemical potential control can modulate the LSPR energy which induces the

strong coupling region.

In the cavity quantum electronic dynamics, the coupling between plasmonic structure and

excitons of dye molecules or quantum dots have been evaluated by classical-mechanical model[27].

These result were well recurrence of the finite difference time domain calculations[27]. Then, I adopted

the classical coupled-oscillator model to analyze the spectral feature. Both oscillators are coupled through the electric near-field with coupling energy $\hbar g = |\langle \mathbf{d} \cdot \mathbf{E} \rangle|$, where $\mathbf{d}$ represents electric dipole due to electronic transition resonance of a molecule and $\mathbf{E}$ represents a electric dipole due to plasmonic resonance at enhanced field the metal surface. The equation of motion for the two oscillators are

$$\frac{\partial^2 x_{LSP}(t)}{\partial t^2} + \gamma_{LSP} \frac{\partial x_{LSP}(t)}{\partial t} + \omega_{LSP}^2 x_{LSP}(t) + g \frac{\partial x_{HITC}(t)}{\partial t} = F_{LSP}(t) \tag{6.5}$$

$$\frac{\partial^2 x_{HITC}(t)}{\partial t^2} + \gamma_{HITC} \frac{\partial x_{HITC}(t)}{\partial t} + \omega_{HITC}^2 x_{HITC}(t) - g \frac{\partial x_{LSP}(t)}{\partial t} = F_{HITC}(t) \tag{6.6}$$

where x_{LSP} and x_{HITC} are the coordinates of plasmonic and HITC electronic oscillation, respectively, γ_{LSP} and γ_{HITC} are a line-width of plasmonic and HITC electronic resonance respectively, ω_{LSP} and ω_{HITC} are resonance frequency of plasmon and that of HITC electronic transition, respectively, and F_{LSP} and F_{HITC} represent the driving forces of the two oscillators, respectively. I set $F_{HITC}(t) = 0$, because the molecular extinction cross section is negligible compared to that of the Au nanoparticle, $F_{LSP} << F_{HITC}(t)$. I can describe extinction cross-section

$$C_{ext}(\omega) \propto \omega \operatorname{Im}\left(\frac{\left(\omega_{HITC}^2 - \omega^2 - i\gamma_{HITC}\omega \right)}{\left(\omega^2 - \omega_{LSP}^2 + i\gamma_{LSP}\omega \right)\left(\omega^2 - \omega_{HITC}^2 + i\gamma_{HITC}\omega \right) - \omega^2 g^2} \right) \tag{6.7}$$

To make clear the physical insight of Eq. (6.7), the formula can be deformed under resonant condition $\omega_0 = \omega_{LSP} = \omega_{HITC}$ as

$$C_{ext}(\omega) \propto \omega \operatorname{Im}\left(\frac{\omega_0 - \omega - i\gamma_{HITC}\omega/2}{2\omega_0 \sqrt{g^2 - \left(\gamma_{LSP} - \gamma_{HITC} \right)^2/4}} \left(\frac{1}{\omega - \Omega_+} - \frac{1}{\omega - \Omega_-} \right) \right) \tag{6.8}$$

81

where $\Omega_\pm = \omega_0 + i(\gamma_{LSP} + \gamma_{HITC})/4 \pm \sqrt{g^2/4 - (\gamma_{LSP} - \gamma_{HITC})^2/16}$. I simulated the spectral

properties in Figure 6.4 by using the peak position of LSP energy and linewidth , HITC energy and

linewidth. Peak positions of experimental extinction spectra were fitted by Lorentzian function.

Simulated spectra were shown in Figure 6.4 (d, e, f) which are well reappearance. Spectral feature

were simulated by changing the value of g. Then I could obtain the coupling strength g which is

shown in Figure 6.5. From +0.3 V to -0.5 V, values of g were constant around $0.15 - 0.20$ eV, then g

value were diminished in the area from -0.5 V to -0.9 V. Value of g (c) is determined by electric

dipole due to electronic transition resonance of a molecule and electric dipole due to plasmonic

resonance at enhanced field the metal surface. In my system, electric dipole is assumed to constant

among each electrochemical potential region because intrinsic Au nanostructures are used. The

diminished value of g at negative potential region (from -0.5 V to -0.9 V) may reflect the chance of

electric dipole due to electronic transition resonance of a molecule. It is known that the reduction

potential of HITC molecules are at -0.5 V (vs Ag/AgCl)[28]. Fluctuations of orientation and adsorbed

structure of molecules on the metal surface caused diminished value of g. In the electrochemical

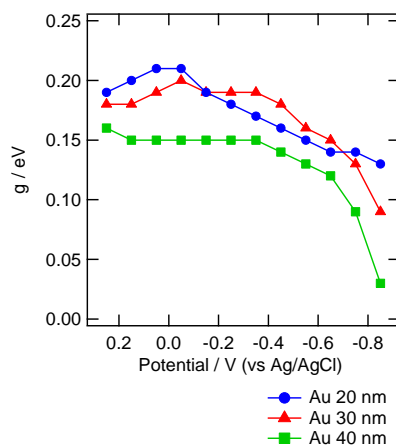potential region from +0.3 V to -0.5 V, I succeeded to tune the LSP energy against the energy of

Figure 6.5 g values against the electrochemical potential.

exciton of HITC. To evaluate the molecular fluctuation, surface enhanced Raman scattering is desirable tool for measure. Then in-situ electrochemical Raman measurement was performed.

Figure 6.6 show the Raman spectra under electrochemical potential control. Observed Raman band were 133 and 298 cm^{-1} which are assigned to the molecule's structural vibrations, and 501, 554, 797, 929 and 1126 cm^{-1} which are assigned to the C-C stretching mode and the mode are same as powder of HITC. The vibrational modes of 133 cm^{-1} provide the intensity modulation at each electrochemical potential.

At the negative potential region, Raman spectra were fluctuated. Fluctuated spectra at -0.6 V were shown in Figure 6.7 (a). Background of Raman spectrum especially changed although band intensity at 133 cm^{-1} was stable. Then Raman spectra were divided into intensity of Raman band at 133 cm^{-1} (I_{133}) and intensity of background (I_{BG}). In Figure 6.7 (b), the Raman intensity at 133 cm^{-1} and background intensity of Au30@HITC were plotted as a function of time. The scan from positive potential to negative potential promotes the fluctuation of the Raman intensity. The reduction potential of HITC molecules are known at -0.5 V (vs Ag/AgCl)[28]. At the more negative of the reduction potential region it seems to diffuse of the adsorbed molecules on the metal surface. In the
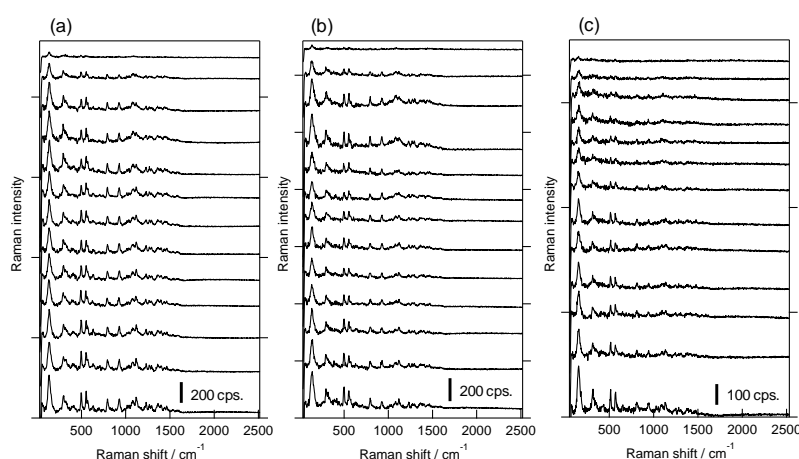

Figure 6.6 Raman spectra under electrochemical potential control : Au20@HITC (a), Au30@HITC (b), Au40@HITC (c), excitation power I_{ex} = 50 μW, and exposure time t_{sec} = 1 s.

electrochemical tuning of energy at LSP resonance, fluctuations of the band intensity were measured.

As shown in the Raman spectra, background of Raman spectra was mainly fluctuated. As shown in Figure 6.8, background intensity and Raman intensity were analyzed at each substrate. In Figure 6.8 (a, b) intensity of background were mainly fluctuated than the intensity of Raman. Especially in Figure 6.8 (b), fluctuation of intensity of background was highest at the Au30 substrate. At the -0.2 V which is more positive than potential of reduction, fluctuation of intensity of Raman band and intensity of background were both repressed as shown in Figure 6.8 (c, d). Au30 was resonant with exciton of dye molecules at negative potential region which achieved the strong coupling regime. The resonant condition induced the enhancement of the background

For molecular optical transition which is resonant with excitation energy, surface-enhanced resonant Raman scattering (SERRS) is usually accompanied by surface enhanced fluorescent (SEF) as represented in background. SERRS and SEF were both considered by electromagnetic effect which is caused by plasmon[29-33]. The blinking and fluctuation of SERRS and
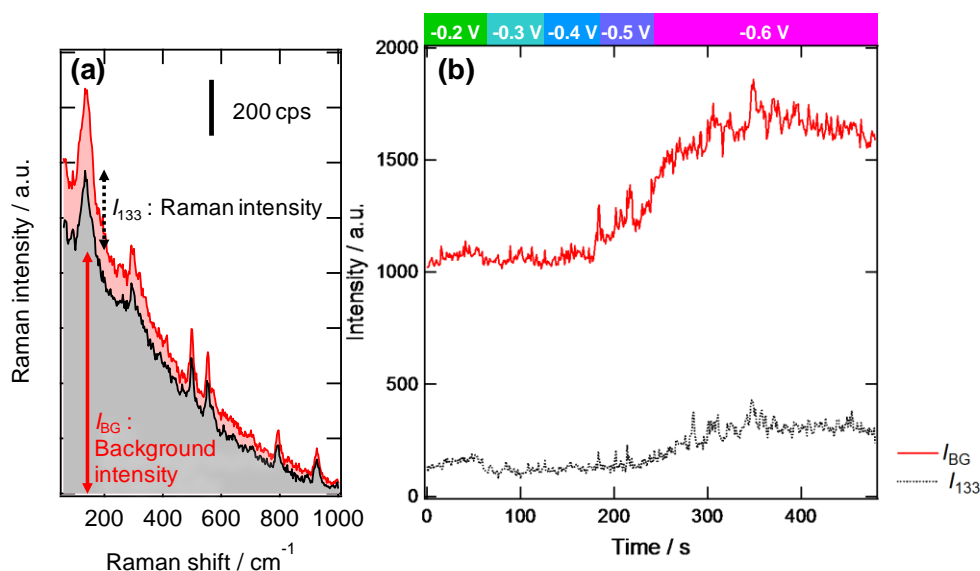

Figure 6.7 Raman spectra at -0.6 V at 300 s (a, black spectrum) and 330 s (a, red spectrum), time course of Raman intensity (b, red solid line) and backscattering intensity (b, black dotted line).

SEF feature were also measured[34-36]. It is known that the origin of fluctuation of background is come from changes in the orientation of dipole axis of molecules to the localized EM field and/or distance between molecules and metal surface[37-39]. In Figure 6.8, increments of Raman and background intensity occurred in several tens of second time scale which is likely to corresponding to molecular diffusive motions changing their orientation and the distance from metal surface.

Additionally, in Figure 6.8 (b), the intensity of background at Au30 especially showed larger fluctuations than the other substrate. In the strong coupling regime, perturbation by photons to molecules is strongly confined in molecule scale[7], because of increment in absorption intensity. Enhanced absorption cross section could induce the effect of the optical trapping of molecules near the metal nano-dimer. As a consequence, moving of molecular position caused the changing of the
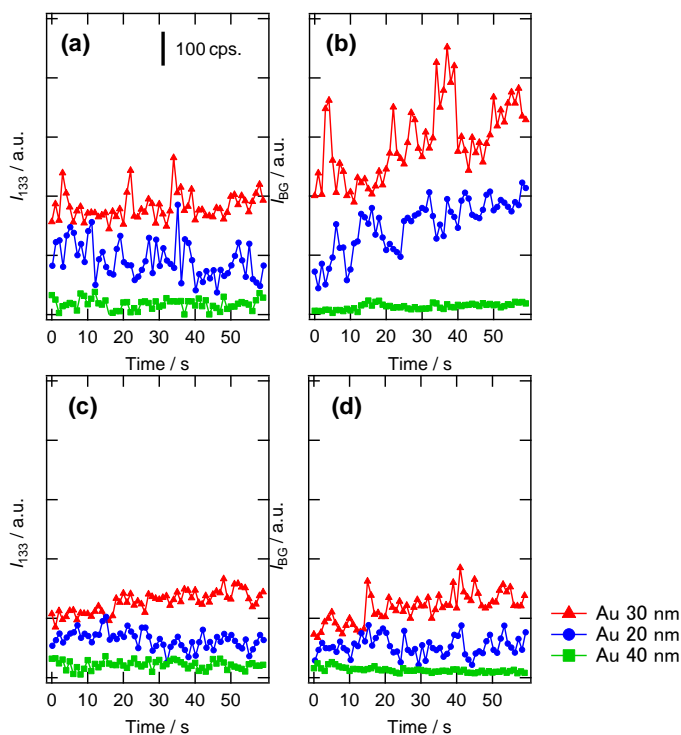

Figure 6.8 Time course of Raman intensity (a, c) and backscattering intensity (b, d) at -0.2 V (c, d) and -0.6 V (a, b). Au deposition thickness were 20 nm (blue circle), 30 nm (red triangle), 40 nm (green square).

coupling strength g ($\hbar g = \left| \langle \mathbf{d} \cdot \mathbf{E} \rangle \right|$) which is concerning about the molecular orientation. Background which is reflected by extinction spectral shape of strong coupling state seems to sensitive to the molecular position and orientation. Although another effects due to heat, photo-bleaching, photo-induced charge transfer between metal and molecules, etc., may also contribute to background fluctuation, apparent effect of the electrochemical potential at the present system strongly supports the importance of the strong coupling tuned by LSP energy to manipulate molecule at the vicinity of metal nanostructure.

6.4. Conclusion

Under the control of the electrochemical potential of the system in the strong coupling regime, LSPR band energy is tuned by changing the density of the free electrons. As maintained the surrounded environment by the adsorbed molecules on the metal surface under potential control, strong coupling behavior was analyzed. The switching between weak coupling regime and strong coupling regime was observed. This technique realizes the evaluation and control of the coupling behavior without changing of coverage of dye molecules. Raman enhancement also measured when the resonant between the polariton states by strong coupling and Raman excitation energy was satisfied. This becomes the first technique for tuning the energy between the LSPR and dye molecular exciton at the same system. The possibility of tuning the coupling strength would provide the insight for the controlling of the photoexcitation state.

6.5 References

1.   Kometani, N.; Tsubonishi, M.; Fujita, T.; Asami, K.; Yonezawa, Y. *Langmuir* **2001,** 17, 578-580.

2.   Franzen, S.; Folmer, J. C. W.; Glomm, W. R.; O'Neal, R. *J. Phys. Chem. A* **2002,** 106, 6533-6540.

3.   Wurtz, G. A.; Evans, P. R.; Hendren, W.; Atkinson, R.; Dickson, W.; Pollard, R. J.; Zayats, A. V.; Harrison, W.; Bower, C. *Nano Lett.* **2007,** 7, 1297-1303.

4.   Fofang, N. T.; Park, T. H.; Neumann, O.; Mirin, N. A.; Nordlander, P.; Halas, N. J. *Nano Lett.* **2008,** 8, 3481-3487.

5.   Ni, W. H.; Yang, Z.; Chen, H. J.; Li, L.; Wang, J. F. *J. Am. Chem. Soc.* **2008,** 130, 6692.

6.   Cade, N.; Ritman-Meer, T.; Richards, D. *Phys. Rev. B* **2009,** 79, 241404.

7.   Ni, W.; Ambjornsson, T.; Apell, S. P.; Chen, H.; Wang, J. *Nano Lett.* **2010,** 10, 77-84.

8.   Hao, Y.-W.; Wang, H.-Y.; Jiang, Y.; Chen, Q.-D.; Ueno, K.; Wang, W.-Q.; Misawa, H.; Sun, H.-B. *Angew. Chem.* **2011,** 123, 7970-7974.

9.   Fofang, N. T.; Grady, N. K.; Fan, Z.; Govorov, A. O.; Halas, N. J. *Nano Lett.* **2011,** 11, 1556-60.

10.   Bonnand, C.; Bellessa, J.; Plenet, J. *Phys. Rev. B* **2006,** 73, 266808.

11.   Balci, S.; Kocabas, C.; Ates, S.; Karademir, E.; Salihoglu, O.; Aydinli, A. *Phys. Rev. B* **2012,** 86, 235402.

12.   Dintinger, J.; Klein, S.; Bustos, F.; Barnes, W.; Ebbesen, T. *Phys. Rev. B* **2005,** 71, 035424.

13.   Vasa, P.; Pomraenke, R.; Cirmi, G.; De Re, E.; Wang, W.; Schwieger, S.; Leipold, D.; Runge, E.; Cerullo, G.; Lienau, C. *ACS Nano* **2010,** 4, 7559-7565.

14.   Salomon, A.; Gordon, R. J.; Prior, Y.; Seideman, T.; Sukharev, M. *Phys. Rev. Lett.* **2012,** 109, 073002.

15.   Bellessa, J.; Bonnand, C.; Plenet, J.; Mugnier, J. *Phys. Rev. Lett.* **2004,** 93, 036404.

16.   Hakala, T. K.; Toppari, J. J.; Kuzyk, A.; Pettersson, M.; Tikkanen, H.; Kunttu, H.; Torma, P. *Phys. Rev. Lett.* **2009,** 103, 053602.

17.   Symonds, C.; Bonnand, C.; Plenet, J. C.; Brehier, A.; Parashkov, R.; Lauret, J. S.; Deleporte, E.; Bellessa, J. *New J. Phys.* **2008,** 10, 065017.

18.   Fontcuberta i Morral, A.; Stellacci, F. *Nature Mater.* **2012,** 11, 272-273.

19.   Hutchison, J. A.; Liscio, A.; Schwartz, T.; Canaguier-Durand, A.; Genet, C.; Palermo, V.; Samori, P.; Ebbesen, T. W. *Adv. Mater.* **2013,** 25, 2481-2485.

20.   Canaguier-Durand, A.; Devaux, E.; George, J.; Pang, Y.; Hutchison, J. A.; Schwartz, T.; Genet, C.; Wilhelms, N.; Lehn, J.-M.; Ebbesen, T. W. *Angew. Chem.* **2013,** 125, 10727-10730.

21.   Schwartz, T.; Hutchison, J. A.; Genet, C.; Ebbesen, T. W. *Phys. Rev. Lett.* **2011,** 106, 196405.

22.   Baudrion, A. L.; Perron, A.; Veltri, A.; Bouhelier, A.; Adam, P. M.; Bachelot, R. *Nano Lett.* **2013,** 13, 282-286.

23.   Berrier, A.; Cools, R.; Arnold, C.; Offermans, P.; Crego-Calama, M.; Brongersma, S. H.; Gomez-Rivas, J. *ACS Nano* **2011,** 5, 6226-6232.

24.   Templeton, A. C.; Pietron, J. J.; Murray, R. W.; Mulvaney, P. *J. Phys. Chem. B* **1999,** 104, 564-570.

25.   Mulvaney, P., Metal Nanoparticles: Double Layers, Optical Properties, and Electrochemistry. In *Nanoscale Materials in Chemistry*, John Wiley & Sons, Inc.: 2002; pp 121-167.

26.   Ali, A. H.; Luther, R. J.; Foss Jr, C. A.; Chapman, G. B. *Nanostruct. Mater.* **1997,** 9, 559-562.

27.   Wu, X.; Gray, S. K.; Pelton, M. *Opt. Express* **2010,** 18, 23633-23645.

28.   Yau, C. M. S.; Pascu, S. I.; Odom, S. A.; Warren, J. E.; Klotz, E. J. F.; Frampton, M. J.; Williams, C. C.; Coropceanu, V.; Kuimova, M. K.; Phillips, D.; Barlow, S.; Bredas, J.-L.; Marder, S. R.; Millar, V.; Anderson, H. L. *Chem. Commun.* **2008,** 2897-2899.

29.   Moskovits, M. *Rev. Mod. Phys.* **1985,** 57, 783-826.

30.   Inoue, M.; Ohtaka, K. *J. Phys. Soc. Jpn.* **1983,** 52, 3853-3864.

31.   Pettinger, B. *J. Chem. Phys.* **1986,** 85, 7442-7451.

32.   Johansson, P.; Xu, H.; Käll, M. *Phys. Rev. B* **2005,** 72, 035427.

33.   Yoshida, K.-i.; Itoh, T.; Tamaru, H.; Biju, V.; Ishikawa, M.; Ozaki, Y. *Phys. Rev. B* **2010,** 81, 115406.

34.   Galloway, C. M.; Etchegoin, P. G.; Le Ru, E. C. *Phys. Rev. Lett.* **2009,** 103, 063003.

35.   Etchegoin, P. G.; Le Ru, E. C. *Anal. Chem.* **2010,** 82, 2888-2892.

36.   Itoh, T.; Iga, M.; Tamaru, H.; Yoshida, K.-i.; Biju, V.; Ishikawa, M. *J. Chem. Phys.* **2012,** 136,024703.

37.   Ringler, M.; Schwemer, A.; Wunderlich, M.; Nichtl, A.; Kürzinger, K.; Klar, T. A.; Feldmann, J. *Phys. Rev. Lett.* **2008,** 100, 203002.

38.   Chen, Y.; Munechika, K.; Ginger, D. S. *Nano Lett.* **2007,** 7, 690-696.

39.   Takimoto, B.; Nabika, H.; Murakoshi, K. *J. Phys. Chem. C* **2009,** 113, 11751-11755.

Chapter 7

General Conclusion

In this thesis, I developed the systems to open up the way for novel photoexcitaion processes based on the findings obtained from in-situ observation of the systems in which localized surface plasmon (LSP) and molecules interact strongly. It has been found that the use of localized surface plasmon which is used as highly confined, localized and anisotropic light source was appropriate and relevant for evaluating and controlling the interaction. The highly-ordered metal nanostructure provided the possibilities of anisotropic photoexcitation at interface were suggested. The optimization of system, which is confirmation of the singularities of analyte, evaluation of the structures and controlling of the electrochemical potential of the metal surface, was figured out the anisotropic excitation from LSP and additional transition for photoexcitation process. Furthermore, excited electronic energy states were modulated by the strong coupling between LSP and excitons of molecules. This developed feature of electronic structure was active controlled by electrochemical potential. The construction of the developed electronic structure systems pave the way for the plasmon-induced photoexcitation processes. The main results can be summarized as follows.

First, the Ag nano-dimer structure was fabricated for the polarized SERS measurement (Chapter 2). The polarized surface-enhanced Raman scattering (SERS) were performed in the 4,4'-bipyridine (44bpy) solution. Depolarized SERS signals were obtained at the specific band intensity ratio of Raman spectrum. I performed the evaluation of the single crystal 44bpy structure and the Raman tensor which indicate the Raman activity. By comparing the result of DFT calculation, it is found that Raman intensity ratio represent the adsorbed molecular orientation on the

metal surface. The SERS depolarization at specific adsorption states of molecules implies that the interface between molecuce and metal induce the anisotropic photoexcitation. For evaluation of the photoexcitation process, I performed single molecular measurement (Chapter 3) and the measurement under electrochemical potential tuning (Chapter 4). The single molecule Raman measurement was achieved by the conductance measurement simultaneously. The metal nanojunction was prepared by electron beam lithography and sputtering methods. The conductance between the metal nanojunction clarified the number of molecules and the strength of adsorption. The charge transfer from metal to molecules provides the additional electronic resonant condition to excitation energy. The resonant like condition of Raman process showed the enhancement of additional vibrational mode which is not observed in the normal Raman condition. This Raman process apparent showed the anisotropic excitation at the interface between molecules and metal. Then the system was developed to the single walled carbon nanotube (SWNT) measurement under electrochemical potential tuning. The SWNT is appropriate for evaluation of the electronic excitation process because of its electrochemical doping feature and the anisotropic electronic excitation properties. The depolarized Raman scattering was acquired. Additional electronic excitation was evident by the Raman active mode. Thus the evaluation of the singularities and electronic state provide the possibilities that the excitation by the different energy cause the anisotropic polarized properties.

Next, the strong coupling regime was achieved by using LSP and molecular excitons, which induce the modulation of the electronic state (Chapter 5). The system was controlled by changing the LSP energy against the dye exciton. The resonant condition between LSP and dye exciton energy show hybridized state and energy separation. Hybridized state was suggested to use for the new electronic excitation state. Highly polarized SERS signal was acquired in the hybridized system. And Raman intensity was enhanced at the resonant condition between the hybrid states and

the excitation. This show the molecules in the confined electromagnetic field provide the hybridized state. In addition, the energy state of strong coupling was tuned in the electrochemical environment (Chapter 6). By tuning the electrochemical potential, LSP energy was controlled associated with the free electron density of nanostructure. As maintained at the environment of the strong coupling system, such as nanostructure size and the number of layered dye, coupling strength was tuned. The developed hybridized state was well controlled, and represent the electronic excitation process were also controlled.

In conclusion, above investigations about newly developed electronic state represented the indispensable perception about the photoexcitation process at the interface between metal and adsorbed molecules. The alternation of the excited state is supposed to realize the new process of the photochemical reaction on the metal surface. This possibility opens the door for us to develop the efficiency, selectivity, and sustainability of various photochemical reactions.

Acknowledgments

March, 2014

Fumika Nagasawa